

Modeling Sleep and Wakefulness in the Thalamocortical System

Sean Hill and Giulio Tononi

Department of Psychiatry, University of Wisconsin—Madison, Madison, Wisconsin

Submitted 1 September 2004; accepted in final form 26 October 2004

Hill, Sean and Giulio Tononi. Modeling sleep and wakefulness in the thalamocortical system. *J Neurophysiol* 93: 1671–1698, 2005. First published November 10, 2004; doi:10.1152/jn.00915.2004. When the brain goes from wakefulness to sleep, cortical neurons begin to undergo slow oscillations in their membrane potential that are synchronized by thalamocortical circuits and reflected in EEG slow waves. To provide a self-consistent account of the transition from wakefulness to sleep and of the generation of sleep slow waves, we have constructed a large-scale computer model that encompasses portions of two visual areas and associated thalamic and reticular thalamic nuclei. Thousands of model neurons, incorporating several intrinsic currents, are interconnected with millions of thalamocortical, corticothalamic, and both intra- and interareal corticocortical connections. In the waking mode, the model exhibits irregular spontaneous firing and selective responses to visual stimuli. In the sleep mode, neuromodulatory changes lead to slow oscillations that closely resemble those observed *in vivo* and *in vitro*. A systematic exploration of the effects of intrinsic currents and network parameters on the initiation, maintenance, and termination of slow oscillations shows the following. 1) An increase in potassium leak conductances is sufficient to trigger the transition from wakefulness to sleep. 2) The activation of persistent sodium currents is sufficient to initiate the up-state of the slow oscillation. 3) A combination of intrinsic and synaptic currents is sufficient to maintain the up-state. 4) Depolarization-activated potassium currents and synaptic depression terminate the up-state. 5) Corticocortical connections synchronize the slow oscillation. The model is the first to integrate intrinsic neuronal properties with detailed thalamocortical anatomy and reproduce neural activity patterns in both wakefulness and sleep, thereby providing a powerful tool to investigate the role of sleep in information transmission and plasticity.

INTRODUCTION

The transition from wakefulness to sleep is accompanied by striking changes in neural activity, which are evident at the level of individual neurons recorded intracellularly as well as at the population level recorded by the electroencephalogram (EEG). During wakefulness, cortical neurons are tonically depolarized and fire at irregular intervals, giving rise to an EEG characterized by low-voltage, fast-activity patterns. With the onset of slow-wave sleep, virtually all cortical neurons undergo a slow oscillation (<1 Hz) in their membrane potential (Steriade 2003). The slow oscillation is composed of a hyperpolarized phase or “down-state” during which neurons are deeply hyperpolarized and remain silent for a few hundred milliseconds. The down-state is followed by a depolarized phase or “up-state,” also lasting several hundred milliseconds, during which neurons fire at rates that are even higher than in quiet wakefulness. These fluctuations in membrane potential are

reflected in the cortical EEG as slow waves of high-voltage activity.

The slow oscillation is the fundamental cellular phenomenon that groups and organizes sleep rhythms such as slow-wave activity and sleep spindles (Steriade 2003). After its discovery in anesthetized cats (Steriade et al. 1993), the slow oscillation has been investigated during natural sleep *in vivo* (Achermann and Borbely 1997; Steriade et al. 2001), in cortical slabs (Timofeev et al. 2000), *in vitro* in cortical slice preparations (Mao et al. 2001; Sanchez-Vives and McCormick 2000), and in computo (Bazhenov et al. 2002; Compte et al. 2003). These studies have revealed that both intrinsic currents and various kinds of synaptic interactions are involved in initiating, maintaining, and terminating the slow oscillation, and that cortico-cortical circuits are involved in synchronizing it (Amzica and Steriade 1995b).

To integrate the information gathered from these different experimental approaches, we have constructed a large-scale model of the thalamocortical system that aims to provide a coherent account of the transition from wakefulness to sleep and the generation of the slow oscillation at several different levels—from ion channel kinetics to global EEG phenomena. The model incorporates key aspects of the neuroanatomical organization of the thalamocortical system, including two visual cortical areas subdivided into multiple layers, corresponding thalamic and reticular sectors, and several millions of intra- and interareal connections linking >65,000 spiking neurons. Moreover, the model incorporates several types of intrinsic conductances (mediating the hyperpolarization-activated cation current I_h , low-threshold calcium current I_T , persistent sodium current $I_{Na(p)}$, potassium leak current I_{KL} , depolarization-dependent potassium current I_{DK} —representing Ca^{2+} and Na^+ -dependent K^+ currents) and synaptic currents [α -amino-3-hydroxy-5-methyl-4-isoxazolepropionic acid (AMPA), *N*-methyl-d-aspartate (NMDA), γ -aminobutyric acid-A (GABA_A), γ -aminobutyric acid-B (GABA_B)].

Because of these properties, the model is able to reproduce experimental data ranging from intracellular traces and multi-unit rasters to optical imaging-like voltage patterns and EEG-like field potentials. Moreover, by simulating changes in intrinsic currents arising from the reduced release of neuromodulators, the model can switch from a waking to a sleep mode of activity. Specifically, in the waking mode the model reproduces spontaneous activity patterns as well as selective responses to visual stimuli that are seen *in vivo*. After transitioning to the sleep mode, the model engages in slow oscillations that closely resemble those observed experimentally. By providing a comprehensive view of all system variables and by

Address for reprint requests and other correspondence: S. Hill, University of Wisconsin—Madison, Department of Psychiatry, 6001 Research Park Boulevard, Madison, WI 53719-1176 (E-mail: seanhill@wisc.edu).

The costs of publication of this article were defrayed in part by the payment of page charges. The article must therefore be hereby marked “advertisement” in accordance with 18 U.S.C. Section 1734 solely to indicate this fact.

permitting idealized “experimental” manipulations, the model provides a self-consistent account of the mechanisms responsible for the initiation, maintenance, and termination of the slow oscillation and of its synchronization within and across thalamocortical circuits.

METHODS

In the next sections, we describe the principles used to construct and scale the simulated cortical and thalamic regions, the layout of the various connection pathways within and among these regions, and the implementation of cellular and synaptic properties. We then describe the sources of spontaneous activity, the procedures for the collection and analysis of data, and the actual computer implementation.

Regional organization

PRIMARY CORTICAL AREA. The model (Fig. 1) is organized in regions and pathways consisting of a primary and a secondary area of visual cortex, two corresponding regions of the dorsal thalamus, and two regions of the reticular thalamic nucleus. The primary visual area (V_p) represents a restricted portion of cat striate cortex (area 17) and

it contains units with small receptive fields that are selective for oriented segments. The simulated cortex is divided into 3 layers with different patterns of afferent, efferent, and local connectivity corresponding to supragranular layers (L2–3), infragranular layers (L5–6), and layer 4 (L4).

In the cat, the striate cortex exhibits a basic periodicity of structure and function at the scale of about 1 mm. This organization is manifested both in terms of the center-to-center distance of isoorientation bands (Kisvarday and Eysel 1993; Kisvarday et al. 1997; Lowel et al. 1987) and in terms of the average separation of neighboring axonal termination patches in supragranular layers (Kisvarday and Eysel 1992). To constrain our model, we assume that an area of roughly 1.0 mm^2 forms a basic macrounit in the striate cortical mosaic array. V_p is scaled to span 64 (8×8) such macrounits. Therefore V_p corresponds to approximately 0.8 cm^2 of striate cortical surface and spans a monocular patch of $8 \times 8^\circ$ in the parafoveal visual field. Each macrounit in the model contains discrete groups of orientation selective cells. In the present model, 2 groups of cells selective for vertical and horizontal oriented input represent a simplified version of the X pathway for one eye.

Figure 2 shows the detailed orientation-selective, feedforward, and feedback circuitry for one horizontally selective and one vertically selective macrounit. Each topographic location (topographic element)

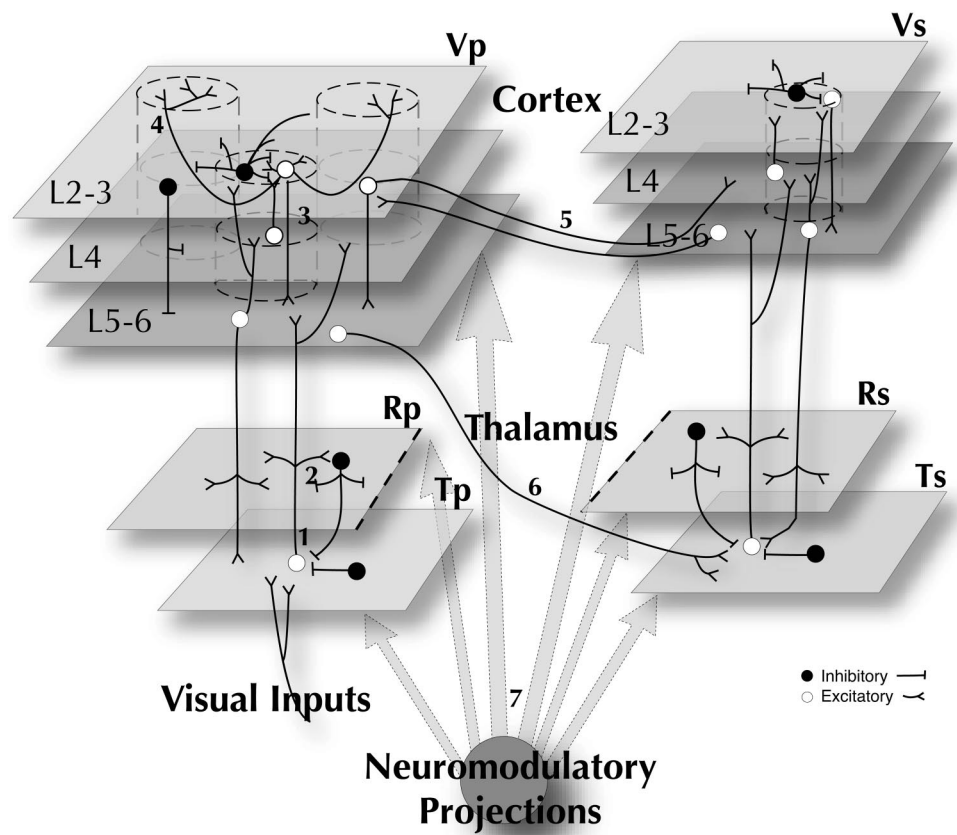


FIG. 1. Schematic of the thalamocortical model. Primary thalamocortical circuit (*left*) including a 3-layered primary visual cortical area (V_p), reticular nucleus (R_p), and dorsal thalamus (T_p) and secondary visual area V_s (with its associated thalamic sectors R_s and T_s) (*right*). Visual inputs (*left*), including spontaneous random optic nerve firing, excite inhibitory (black) and excitatory (white) neurons in the primary thalamus (T_p). (1) Thalamocortical loops: excitatory T_p and T_s neurons project to L4 (corresponding to cortical layer 4) and L5–6 (corresponding to infragranular layers 5–6) cortical neurons and by collaterals to R_p and R_s (corresponding to the reticular nucleus of the thalamus). (2) Reticular nucleus networks: R_p and R_s neurons are part of a dense inhibitory network that sends diffuse inhibitory projections to thalamocortical neurons in T_p and T_s . (3) Cortical interlaminar (vertical) loops: columnar projections are made from L4 to L2–3 (corresponding to supragranular layers 2–3), from L2–3 to L5–6, and from L5–6 back to L4 and L2–3. (4) Cortical intralaminar (horizontal) connections: each layer contains excitatory projections (shown only for L2–3 in V_p) forming connections between patches of cells with similar response selectivity (for horizontal or vertical bars). (5) Interareal corticocortical loops: forward projections from L2–3 of V_p to L4 of V_s ; backward projections from L5–6 of V_s to L2–3 of V_p . (6) Excitatory projections from L5–6 to thalamocortical neurons in T_s . (7) Diffuse neuromodulatory systems project throughout the entire thalamocortical network [corresponding to influences of acetylcholine (ACh), norepinephrine (noradrenaline, NA), 5-hydroxytryptamine (5-HT), etc.]. Not drawn to scale.

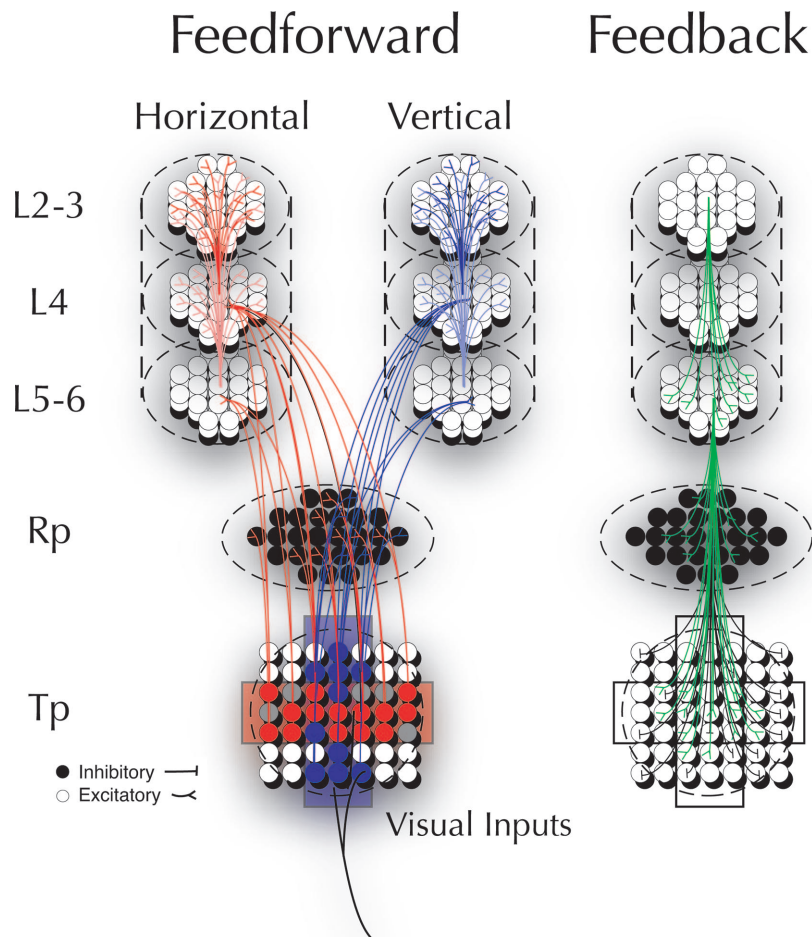


FIG. 2. Schematic of modeled orientation-selective receptive fields, feedforward and feedback projections. Feedforward connections start with visual input to the elements of the model thalamus (Tp). Each topographic element in Tp contains one excitatory (white circle) and one inhibitory (black circle) neuron. Rp contains one inhibitory cell per topographic element. Each topographic element in layers L5–6, L4, and L2–3 consists of 2 excitatory and 1 inhibitory cell. Excitatory cells in Tp project to inhibitory cells in Rp and both excitatory and inhibitory cells in L4 and L5–6. Orientation selectivity is achieved by the convergence of afferents from an oriented rectangular region in Tp onto individual cortical cells in L4 and L5–6. All excitatory cells in L4 and L5–6 receive oriented input from Tp. Red marks the receptive field and projection patterns for a cortical cell selective for horizontal input. Blue marks the receptive field and projection patterns for a cortical excitatory cell selective for vertical input. Feedback connections (shown in green) show the projection pattern from L5–6 to Rp and Tp. These connections are present for both horizontally and vertically selective cells.

in the model cortex is considered to correspond to a cortical column, which is represented by 9 model neurons (2 excitatory and 1 inhibitory for each of the 3 layers). All topographic elements in Vp are organized in maps of 40×40 elements for each of the 2 modeled orientation selectivities (horizontal and vertical). Orientation selectivity is achieved by the convergence of afferents from an oriented rectangular region in Tp onto individual cortical cells in L4 and L5–6. The subdivision of the modeled cortical areas in elements spanning all layers reflects the developmental, anatomical, and physiological evidence for a basic columnar organization of neocortex (Gilbert 1993; Mountcastle 1997, 1957; Rakic 1995).

Assuming that different selectivities are mapped onto nonoverlapping pieces of cortex, and that there are about 62,000 neurons beneath 1 mm^2 of cortical surface in area 17 (Beaulieu and Colonnier 1983), each topographic element corresponds to a cortical column with a surface area of $1,454 \mu\text{m}^2$ and containing approximately 94 neurons. Because we explicitly model only 9 cells for each topographic element, each modeled cell represents the activity of approximately 10 cortical neurons, making the topographical elements in the model comparable to the basic cortical modules proposed by Peters and Payne (1993). Although the ratio of modeled excitatory/inhibitory cells (66%/33%) is not exactly the same as that observed *in vivo* (about 80%/20%) because of computational considerations, the observed ratio of excitatory/inhibitory synapses is maintained (see following text).

SECONDARY CORTICAL AREA. The secondary visual area (Vs) corresponds to an extrastriate area located along the ventral occipitotemporal pathway. Although Vs does not represent in detail any particular region of visual cortex, we use area 21 in the cat as a reference, which is the presumed homolog of cortical area V4 in the monkey (Payne 1993). Vs is assumed to be about half the size of Vp [in the monkey,

V1 is $1,120 \text{ mm}^2$ and V4 is 540 mm^2 (Felleman and Van Essen 1991)]. In the model, Versus is based on some general properties associated with extrastriate areas (e.g., an enlargement of receptive fields) and with termination patterns of “forward” and “backward” corticocortical projections (Felleman and Van Essen 1991; Van Essen et al. 1992). Vs contains neurons that are selective for either vertical lines, horizontal lines, or line crossings, organized in a coarse topographic map. For each of its 3 selectivities, Vs has a map of 30×30 elements (for a total of 24,300 model neurons) as compared with the 40×40 (totaling 28,800 model neurons) elements in Vp.

THALAMIC SECTORS. According to Peters and Payne (1993), there is a rough correspondence between the number of X-cells in the lateral geniculate nucleus (LGN) and the number of basic cortical modules in area 17. We therefore model a geniculate map (Tp) composed of the same number of elements (40×40) as Vp. Each element of Tp contains 2 modeled neurons that correspond respectively to an X-relay cell and to an inhibitory interneuron. For simplicity of implementation, only the on-portion of thalamic receptive fields is modeled. The secondary thalamic map (Ts) has 30×30 elements and its visuotopic arrangement has a much lower spatial resolution than that of Tp. Two sectors of the reticular nucleus, primary perigeniculate (Rp) and secondary higher-order (Rs), are modeled respectively as a 40×40 and a 30×30 map of inhibitory neurons.

Connectivity

In constructing the model, special emphasis was placed on the incorporation of realistic network properties, such as the spread and relative proportions of the various sets of connections composing the intra- and interregional thalamocortical circuitry. Specific patterns of

arborization are classified as either *focused* or *diffuse*, on the basis of anatomical data. The focused connection pattern diverges for single arbors over a topographically registered region with a diameter of 5 target elements. Diffuse projections typically cover an area with a diameter of 25 elements for a single arbor. Contacts from individual arbors in the target area are made probabilistically according to Gaussian spatial density profiles. The proportion of synapses from different sources was used as a constraint in the parameterization of the various density profiles (Table 1). Two books, by Sherman and Guillery (2001) and White and Keller (1989), were particularly helpful in the development of this model.

VERTICAL INTERLAMINAR CONNECTIONS. Interlaminar connections couple neurons vertically through the cortical depth. These connections may be described as part of a loop that includes the following major steps (Gilbert 1993; Mountcastle 1997): from layer IV to supragranular layers, from supragranular to infragranular layers, and from infragranular back to layer IV and to supragranular layers (Callaway and Wiser 1996; Wiser and Callaway 1996, 1997). All these projections are made in a focused manner in the model. As a further constraint, we consider the proportion of synapses from different sources in each layer. As an example, for each simulated excitatory cell of layer IV, there are on average 40 interlaminar connections from infragranular layer and 23 intralaminar connections from layer IV, in close agreement with the 45% ratio reported in the cat striate cortex (Ahmed et al. 1994). A similar connectivity was established in each map of Versus.

HORIZONTAL INTRALAMINAR CONNECTIONS. Individual excitatory neurons in the supragranular layers of striate cortex have intralaminar horizontal projections that tend to be organized in patches of 200–400 mm in diameter. These patches typically interconnect neurons that have similar orientation preference (Kisvarday et al. 1997). Patches originating from a single location extend over a region of roughly 2–4 mm (Gilbert 1993). In the model, horizontal connections in the supragranular layer of Vp are made diffusely onto isoorientation cells, with an equivalent spread of $5.5 \times 5.5 \text{ mm}^2$. Intrinsic connections in the infragranular layer of Vp have a similar organization. Intralaminar connections in layer IV extend over a more limited area with a diameter of 15 elements. This reduced projective field reflects the more compact arborization in layer IV (Douglas and Martin 2003).

INTRACORTICAL INHIBITORY CONNECTIONS. The cerebral cortex contains many different types of GABAergic inhibitory interneurons (Douglas and Martin 2003; Jones 1993). Among these, basket cells are ubiquitous and project mostly to the same layer where their soma is located. Double-bouquet cells are concentrated in supragranular layers (Conde et al. 1994; Kawaguchi 1995; Kawaguchi and Kubota 1997; Peters and Sethares 1997) and their projections are organized in a restricted columnar arrangement that extends to most layers. There are indications that basket cells and other inhibitory interneurons act through fast GABA_A-receptors, whereas double-bouquet cells may preferentially activate GABA_B receptors (Kang et al. 1994). In the model, basketlike cells provide a fast (GABA_A-like) inhibition within each cortical layer to all cell types; double-bouquet analogs located in supragranular layers provide a slow (GABA_B-like) inhibitory control of a narrow cylinder extended to all 3 layers.

The relationship between inhibition and orientation selectivity in the visual cortex is complex. However, some recent studies suggest that a single basket cell in the cat visual cortex provides input to surrounding regions representing the whole range of orientations, including iso- and cross-orientations to that basket cell soma (Kisvarday and Eysel 1993; Kisvarday et al. 1994). In the model, we assume that lateral inhibition (GABA_A) is provided equally to both of the modeled orientation selectivities in Vp. In Vs, half of the terminals of individual basketlike cells in Vs provide input to cells with similar selectivity to that of the parent soma, whereas the remaining half are split evenly between cells of other selectivities. The density profile of

inhibitory connections was adjusted such that the relative proportions of inhibitory connections per layer are comparable to the values reported in the literature (i.e., about 10–20% of all synapses) (Beaulieu and Colonnier 1985; Beaulieu et al. 1992).

FORWARD AND BACKWARD INTERAREAL CONNECTIONS. According to several studies, backward connections are considerably more divergent than forward connections. This has been documented for projections from area MT to V1 and V2 of primates (Krubitzer and Kaas 1989; Rockland and Knutson 2000; Shipp and Zeki 1989; Zeki and Shipp 1989) and from V2 to V1 (Henry et al. 1991; Rockland and Van Hoesen 1994; Rockland and Virga 1989). Reconstructions of single axons indicate that forward projections from V1 and V2 (Rockland 1992; Rockland and Knutson 2000; Rockland and Virga 1989) to V4 have discrete terminal clusters (2–4 clusters per axon, 250 mm wide), which are distributed over 2 to 2.5 mm. Conversely, individual axons from V4 to V1 diverge $\leq 5 \text{ mm}$ (Rockland et al. 1994). These values should be compared with values around 2 to 5 mm for horizontal connections in V1. According to a classic description, forward projections tend to originate in superficial layers and to terminate in layer 4, whereas backward connections tend to originate from infragranular as well as supragranular layers and to terminate outside layer 4 (Rockland and Pandya 1979). This basic scheme has since become considerably more complicated (Felleman and Van Essen 1991; Maunsell and van Essen 1983). However, in the model, forward connections originating from the supragranular layer of Vp defined the 3 feature-specific responses in Vs. These selectivities resulted from biased convergent projections onto individual L4 neurons of Versus from either a 19×3 region of vertical selective cells, a 3×19 region of horizontal selective cells, or from both selectivities of Vp (9×3 and 3×9 regions, respectively). Backward projections from vertical and horizontal selective cells of Vs originate in the infragranular layer and terminate diffusely in the supragranular layer of Vp, targeting cells of similar orientation specificity. In contrast, backward projections from cross-selective cells extend to both selectivities in Vp. The laminar specificity of projections between Vp and Vs was consistent with that observed between cat areas 17 and 21 (Rosenquist 1985).

THALAMIC CONNECTIONS. Relay cells in the LGN have strong, driving connections to the cortex, and form collaterals only with the reticular nucleus (RT), whereas interneurons in the LGN inhibit other interneurons as well as relay cells with a focused connectivity pattern. RT neurons make diffuse connections within the RT nucleus and to thalamic relay nuclei (Dubin and Cleland 1977). In the model, local interneurons produce (fast) GABA_A-mediated inhibitory postsynaptic potentials (IPSPs) in thalamocortical relay cells. Thalamic to reticular projections (i.e., from Tp to Rp and from Ts to Rs) are made according to the focused connection scheme. RT projections target their corresponding relay sectors of the thalamus in a diffuse manner. Both GABA_A and GABA_B IPSPs mediate the RT inhibition of thalamic relay and interneurons, in accord with the inhibitory effect observed when RT cells fire tonically (Kim and McCormick 1998; Kim et al. 1997; Pinault and Deschenes 1992).

THALAMOCORTICAL AND CORTICOTHALAMIC CONNECTIONS. X-cells in cat laminae A and A1 of the LGN send axons that terminate mainly in layer IV and VI of area 17 (Freund et al. 1989; LeVay and Gilbert 1976; Leventhal 1979). In the model, each simulated cell in L4 of Vp received connections selected from an 8×2 region of the thalamic map for the vertical selectivity (2×8 for the horizontal selectivity). Infragranular cells received about half as many connections from the same geniculate regions. The convergence of projections from these horizontal or vertical patches within the thalamus promoted orientation-specific responses in the cortex. Note that, in the model, the same X-cell targets both horizontal and vertical cortical cells, such that its arbor extends over at least half of an orientation cycle or 0.55 mm. This dimension is consistent with anatomical

TABLE 1. Parameters for the connectivity profiles used to construct the thalamocortical network

Source Area	Source Layer	Cell Type	Target Area	Target Layer	Cell Type	Transmitter	Style	P_{max}	σ	Radius	Strength	Mean Delay
<i>Primary visual area (Vp)</i>												
Horizontal intralaminar connections												
Vp	L2–3	E(V)	Vp	L2–3	E(V)	NMDA	Gaussian	0.05	7.5	12	1	2 ± 0.25
Vp	L2–3	E(V)	Vp	L2–3	E(V)	AMPA	Gaussian	0.05	7.5	12	1	2 ± 0.25
Vp	L2–3	E(V)	Vp	L2–3	I(V)	AMPA	Gaussian	0.05	7.5	12	1	2 ± 0.25
Vp	L4	E(V)	Vp	L4	E(V)	AMPA	Gaussian	0.05	7.5	7	1	2 ± 0.25
Vp	L4	E(V)	Vp	L4	I(V)	AMPA	Gaussian	0.05	7.5	7	1	2 ± 0.25
Vp	L5–6	E(V)	Vp	L5–6	E(V)	AMPA	Gaussian	0.05	7.5	12	1	2 ± 0.25
Vp	L5–6	E(V)	Vp	L5–6	I(V)	AMPA	Gaussian	0.05	7.5	12	1	2 ± 0.25
Vertical interlaminar connections												
Vp	L2–3	E(V)	Vp	L5–6	E(V)	NMDA	Gaussian	1	7.5	2	1	2 ± 0.25
Vp	L2–3	E(V)	Vp	L5–6	E(V)	AMPA	Gaussian	1	7.5	2	1	2 ± 0.25
Vp	L2–3	E(V)	Vp	L5–6	I(V)	AMPA	Gaussian	1	7.5	2	1	2 ± 0.25
Vp	L4	E(V)	Vp	L2–3	E(V)	AMPA	Gaussian	1	7.5	2	2	2 ± 0.25
Vp	L4	E(V)	Vp	L2–3	I(V)	AMPA	Gaussian	1	7.5	2	2	2 ± 0.25
Vp	L5–6	E(V)	Vp	L2–3	E(V)	AMPA	Gaussian	1	7.5	2	2	2 ± 0.25
Vp	L5–6	E(V)	Vp	L2–3	I(V)	AMPA	Gaussian	1	7.5	2	2	2 ± 0.25
Vp	L5–6	E(V)	Vp	L4	E(V)	AMPA	Gaussian	1	7.5	2	2	2 ± 0.25
Vp	L5–6	E(V)	Vp	L4	I(V)	AMPA	Gaussian	1	7.5	2	2	2 ± 0.25
Intracortical inhibitory connections												
Vp	L2–3	I(V)	Vp	L2–3	E(V)	GABA _B	Constant	0.3		1	1	2 ± 0.25
Vp	L2–3	I(V)	Vp	L4	E(V)	GABA _B	Constant	0.3		1	1	2 ± 0.25
Vp	L2–3	I(V)	Vp	L5–6	E(V)	GABA _B	Constant	0.3		1	1	2 ± 0.25
Vp	L2–3	I(V)	Vp	L2–3	E(V)	GABA _A	Gaussian	0.25	7.5	7	1	2 ± 0.25
Vp	L2–3	I(V)	Vp	L2–3	E(H)	GABA _A	Gaussian	0.25	7.5	7	1	2 ± 0.25
Vp	L2–3	I(V)	Vp	L2–3	I(V)	GABA _A	Gaussian	0.25	7.5	7	1	2 ± 0.25
Vp	L2–3	I(V)	Vp	L2–3	I(H)	GABA _A	Gaussian	0.25	7.5	7	1	2 ± 0.25
Vp	L4	I(V)	Vp	L4	E(V)	GABA _A	Gaussian	0.25	7.5	7	1	2 ± 0.25
Vp	L4	I(V)	Vp	L4	E(H)	GABA _A	Gaussian	0.25	7.5	7	1	2 ± 0.25
Vp	L4	I(V)	Vp	L4	I(V)	GABA _A	Gaussian	0.25	7.5	7	1	2 ± 0.25
Vp	L4	I(V)	Vp	L4	I(H)	GABA _A	Gaussian	0.25	7.5	7	1	2 ± 0.25
Vp	L5–6	I(V)	Vp	L5–6	E(V)	GABA _A	Gaussian	0.25	7.5	7	1	2 ± 0.25
Vp	L5–6	I(V)	Vp	L5–6	E(H)	GABA _A	Gaussian	0.25	7.5	7	1	2 ± 0.25
Vp	L5–6	I(V)	Vp	L5–6	I(V)	GABA _A	Gaussian	0.25	7.5	7	1	2 ± 0.25
Vp	L5–6	I(V)	Vp	L5–6	I(H)	GABA _A	Gaussian	0.25	7.5	7	1	2 ± 0.25
<i>Secondary visual area (Vs)</i>												
Horizontal intralaminar connections												
Vs	L2–3	E(V)	Vs	L2–3	E(V)	NMDA	Gaussian	0.05	7.5	12	1	2 ± 0.25
Vs	L2–3	E(V)	Vs	L2–3	E(V)	AMPA	Gaussian	0.05	7.5	12	1	2 ± 0.25
Vs	L2–3	E(V)	Vs	L2–3	I(V)	AMPA	Gaussian	0.05	7.5	12	1	2 ± 0.25
Vs	L4	E(V)	Vs	L4	E(V)	AMPA	Gaussian	0.05	7.5	7	1	2 ± 0.25
Vs	L4	E(V)	Vs	L4	I(V)	AMPA	Gaussian	0.05	7.5	7	1	2 ± 0.25
Vs	L5–6	E(V)	Vs	L5–6	E(V)	AMPA	Gaussian	0.05	7.5	12	1	2 ± 0.25
Vs	L5–6	E(V)	Vs	L5–6	I(V)	AMPA	Gaussian	0.05	7.5	12	1	2 ± 0.25
Vertical interlaminar connections												
Vs	L2–3	E(V)	Vs	L5–6	E(V)	NMDA	Gaussian	1	7.5	2	1	2 ± 0.25
Vs	L2–3	E(V)	Vs	L5–6	E(V)	AMPA	Gaussian	1	7.5	2	1	2 ± 0.25
Vs	L2–3	E(V)	Vs	L5–6	I(V)	AMPA	Gaussian	1	7.5	2	1	2 ± 0.25
Vs	L4	E(V)	Vs	L2–3	E(V)	AMPA	Gaussian	1	7.5	2	2	2 ± 0.25
Vs	L4	E(V)	Vs	L2–3	I(V)	AMPA	Gaussian	1	7.5	2	2	2 ± 0.25
Vs	L5–6	E(V)	Vs	L2–3	E(V)	AMPA	Gaussian	1	7.5	2	2	2 ± 0.25
Vs	L5–6	E(V)	Vs	L2–3	I(V)	AMPA	Gaussian	1	7.5	2	2	2 ± 0.25
Vs	L5–6	E(V)	Vs	L2–3	E(V)	GABA _A	Gaussian	1	7.5	2	2	2 ± 0.25
Vs	L5–6	E(V)	Vs	L2–3	I(V)	GABA _A	Gaussian	1	7.5	2	2	2 ± 0.25
Intracortical inhibitory connections												
Vs	L2–3	I(V)	Vs	L2–3	E(V)	GABA _B	Constant	0.3		1	1	2 ± 0.25
Vs	L2–3	I(V)	Vs	L4	E(V)	GABA _B	Constant	0.3		1	1	2 ± 0.25
Vs	L2–3	I(V)	Vs	L5–6	E(V)	GABA _B	Constant	0.3		1	1	2 ± 0.25
Vs	L2–3	I(V)	Vs	L2–3	E(V)	GABA _A	Gaussian	0.25	7.5	7	1	2 ± 0.25
Vs	L2–3	I(V)	Vs	L2–3	E(C)	GABA _A	Gaussian	0.25	7.5	7	1	2 ± 0.25
Vs	L2–3	I(V)	Vs	L2–3	E(H)	GABA _A	Gaussian	0.25	7.5	7	1	2 ± 0.25
Vs	L2–3	I(V)	Vs	L2–3	I(V)	GABA _A	Gaussian	0.25	7.5	7	1	2 ± 0.25
Vs	L2–3	I(V)	Vs	L2–3	I(C)	GABA _A	Gaussian	0.25	7.5	7	1	2 ± 0.25
Vs	L2–3	I(V)	Vs	L2–3	I(H)	GABA _A	Gaussian	0.25	7.5	7	1	2 ± 0.25
Vs	L4	I(V)	Vs	L4	E(V)	GABA _A	Gaussian	0.25	7.5	7	1	2 ± 0.25
Vs	L4	I(V)	Vs	L4	E(C)	GABA _A	Gaussian	0.25	7.5	7	1	2 ± 0.25
Vs	L4	I(V)	Vs	L4	E(H)	GABA _A	Gaussian	0.25	7.5	7	1	2 ± 0.25

TABLE 1. *continued*

Source Area	Source Layer	Cell Type	Target Area	Target Layer	Cell Type	Transmitter	Style	P_{max}	σ	Radius	Strength	Mean Delay
Vs	L4	I(V)	Vs	L4	I(V)	GABA _A	Gaussian	0.25	7.5	7	1	2 ± 0.25
Vs	L4	I(V)	Vs	L4	I(C)	GABA _A	Gaussian	0.25	7.5	7	1	2 ± 0.25
Vs	L4	I(V)	Vs	L4	I(H)	GABA _A	Gaussian	0.25	7.5	7	1	2 ± 0.25
Vs	L5–6	I(V)	Vs	L5–6	E(V)	GABA _A	Gaussian	0.25	7.5	7	1	2 ± 0.25
Vs	L5–6	I(V)	Vs	L5–6	E(C)	GABA _A	Gaussian	0.25	7.5	7	1	2 ± 0.25
Vs	L5–6	I(V)	Vs	L5–6	E(H)	GABA _A	Gaussian	0.25	7.5	7	1	2 ± 0.25
Vs	L5–6	I(V)	Vs	L5–6	I(V)	GABA _A	Gaussian	0.25	7.5	7	1	2 ± 0.25
Vs	L5–6	I(V)	Vs	L5–6	I(C)	GABA _A	Gaussian	0.25	7.5	7	1	2 ± 0.25
Vs	L5–6	I(V)	Vs	L5–6	I(H)	GABA _A	Gaussian	0.25	7.5	7	1	2 ± 0.25
<i>Interareal connections</i>												
Forward interareal connections												
Vp	L2–3	E(V)	Vs	L4	E(V)	AMPA	Rectangular	0.8		1		3 ± 0.25
Vp	L2–3	E(V)	Vs	L4	I(V)	AMPA	Rectangular	0.8		1		3 ± 0.25
Vp	L2–3	E(H)	Vs	L4	E(H)	AMPA	Rectangular	0.8		1		3 ± 0.25
Vp	L2–3	E(H)	Vs	L4	I(H)	AMPA	Rectangular	0.8		1		3 ± 0.25
Vp	L2–3	E(V)	Vs	L4	E(C)	AMPA	Rectangular	0.8		1		3 ± 0.25
Vp	L2–3	E(V)	Vs	L4	I(C)	AMPA	Rectangular	0.8		1		3 ± 0.25
Vp	L2–3	E(H)	Vs	L4	E(C)	AMPA	Rectangular	0.8		1		3 ± 0.25
Vp	L2–3	E(H)	Vs	L4	I(C)	AMPA	Rectangular	0.8		1		3 ± 0.25
Backward interareal connections												
Vs	L5–6	E(V)	Vp	L2–3	E(V)	NMDA	Gaussian	0.1	7.5	12	1	6 ± 0.5
Vs	L5–6	E(V)	Vp	L2–3	I(V)	AMPA	Gaussian	0.1	7.5	12	1	6 ± 0.5
Vs	L5–6	E(H)	Vp	L2–3	E(H)	NMDA	Gaussian	0.1	7.5	12	1	6 ± 0.5
Vs	L5–6	E(H)	Vp	L2–3	I(H)	AMPA	Gaussian	0.1	7.5	12	1	6 ± 0.5
Vs	L5–6	E(C)	Vp	L2–3	E(V)	NMDA	Gaussian	0.1	7.5	12	1	6 ± 0.5
Vs	L5–6	E(C)	Vp	L2–3	I(V)	AMPA	Gaussian	0.1	7.5	12	1	6 ± 0.5
Vs	L5–6	E(C)	Vp	L2–3	E(H)	NMDA	Gaussian	0.1	7.5	12	1	6 ± 0.5
Vs	L5–6	E(C)	Vp	L2–3	I(H)	AMPA	Gaussian	0.1	7.5	12	1	6 ± 0.5
<i>Thalamus (Tp, Rp, Ts, and Rs)</i>												
Thalamic connections												
Tp	E	Rp		I	AMPA	Gaussian	1	7.5	2	2		2 ± 0.25
Tp	I	Tp		E	GABA _A	Gaussian	0.25	7.5	2	1		2 ± 0.25
Tp	I	Tp		I	GABA _A	Gaussian	0.25	7.5	2	1		2 ± 0.25
Rp	I	Tp		E	GABA _A	Gaussian	0.15	7.5	12	1		2 ± 0.25
Rp	I	Tp		E	GABA _B	Gaussian	0.05	7.5	12	1		2 ± 0.25
Rp	I	Tp		I	GABA _A	Gaussian	0.15	7.5	12	1		2 ± 0.25
Rp	I	Tp		I	GABA _B	Gaussian	0.05	7.5	12	1		2 ± 0.25
Rp	I	Rp		I	GABA _B	Gaussian	0.5	7.5	12	1		2 ± 0.25
Ts	E	Rs		I	AMPA	Gaussian	1	7.5	2	2		2 ± 0.25
Ts	I	Ts		E	GABA _A	Gaussian	0.25	7.5	2	1		2 ± 0.25
Ts	I	Ts		I	GABA _A	Gaussian	0.25	7.5	2	1		2 ± 0.25
Rs	I	Ts		E	GABA _A	Gaussian	0.15	7.5	12	1		2 ± 0.25
Rs	I	Ts		E	GABA _B	Gaussian	0.05	7.5	12	1		2 ± 0.25
Rs	I	Ts		I	GABA _A	Gaussian	0.15	7.5	12	1		2 ± 0.25
Rs	I	Ts		I	GABA _B	Gaussian	0.05	7.5	12	1		2 ± 0.25
Thalamocortical connections												
Tp	E	Vp	L4	E(V)	AMPA	Rectangular	0.50			5		3 ± 0.25
Tp	E	Vp	L4	E(V)	AMPA	Rectangular	0.50			5		3 ± 0.25
Tp	E	Vp	L4	I(V)	AMPA	Gaussian	0.10	7.5	5	5		3 ± 0.25
Tp	E	Vp	L5–6	E(V)	AMPA	Rectangular	0.30			5		3 ± 0.25
Tp	E	Vp	L5–6	E(V)	AMPA	Rectangular	0.30			5		3 ± 0.25
Tp	E	Vp	L5–6	I(V)	AMPA	Gaussian	0.10	7.5	5	5		3 ± 0.25
Tp	E	Vp	L4	E(H)	AMPA	Rectangular	0.50			5		3 ± 0.25
Tp	E	Vp	L4	E(H)	AMPA	Rectangular	0.50			5		3 ± 0.25
Tp	E	Vp	L4	I(H)	AMPA	Gaussian	0.10	7.5	5	5		3 ± 0.25
Tp	E	Vp	L5–6	E(H)	AMPA	Rectangular	0.30			5		3 ± 0.25
Tp	E	Vp	L5–6	E(H)	AMPA	Rectangular	0.30			5		3 ± 0.25
Tp	E	Vp	L5–6	I(H)	AMPA	Gaussian	0.10	7.5	5	5		3 ± 0.25
Corticothalamic connections												
Vp	L5–6	E(V)	Tp	E	AMPA	Gaussian	0.5	7.5	5	1		8 ± 0.5
Vp	L5–6	E(V)	Tp	I	AMPA	Gaussian	0.5	7.5	5	1		8 ± 0.5
Vp	L5–6	E(V)	Rp	I	AMPA	Gaussian	0.5	7.5	5	2.5		8 ± 0.5
Vs	L5–6	E(V)	Ts	E	AMPA	Gaussian	0.5	7.5	5	1		8 ± 0.5
Vs	L5–6	E(V)	Ts	I	AMPA	Gaussian	0.5	7.5	5	1		8 ± 0.5
Vs	L5–6	E(V)	Rs	I	AMPA	Gaussian	0.5	7.5	5	2.5		8 ± 0.5
Vp	L5–6	E(V)	Ts	E	AMPA	Gaussian	1	7.5	2	5		8 ± 0.5

TABLE 1. *continued*

Source Area	Source Layer	Cell Type	Target Area	Target Layer	Cell Type	Transmitter	Style	P_{max}	σ	Radius	Strength	Mean Delay
Vp	L5–6	E(V)	Ts		I	AMPA	Gaussian	1	7.5	2	5	8 ± 0.5
Vp	L5–6	E(H)	Ts		E	AMPA	Gaussian	1	7.5	2	5	8 ± 0.5
Vp	L5–6	E(H)	Ts		I	AMPA	Gaussian	1	7.5	2	5	8 ± 0.5
Thalamic input												
Retina	Optic nerve	E	Tp		E	AMPA	Gaussian	0.75	2.5	1	10	0
Retina	Optic nerve	E	Tp		I	AMPA	Gaussian	0.75	2.5	1	10	0

Connectivity patterns are specified as follows: source area, layer of origin, and cell type (E, excitatory, I, inhibitory) and selectivity (V, vertical; H, horizontal; C, cross); target area, layer of termination, and cell type and selectivity; type of synaptic channel activated by the connection; style of connection pattern (Gaussian: connections are selected according to a Gaussian distribution with a peak of P_{max} and a width of σ , Rectangular: connections are selected by the maximum probability within a rectangular area, Constant-connections are selected according to the maximum probability over the entire radius specified); maximum probability of connection (P_{max}); standard deviation (σ) of the Gaussian distribution used to generate connections (scaled according to the radius); radius of the target area in which the projections from a single source cell diverge (expressed in number of topographic elements along vertical and horizontal axis in target map); strength of the connections (expressed in number of simultaneous PSPs per connection); mean ± SD of the delay of the spike impulse from the source cell to the target cells. Intrinsic cortical connections, corticothalamic projections from Vp to Tp and Rp, thalamocortical and corticothalamic projections from Vs to Ts and Rs, are isomorphic for the various selectivities; as a reference, we give only the connectivity patterns originating from cells selective for vertical orientations. Thalamocortical projections from Tp to Vp and interareal projections are biased and rectangular so as to produce feature selectivities; these projections are described for all the selectivities present in the model.

evidence that X axonal terminals form a single elongated clump in area 17, about 1 mm long × 0.6–0.8 mm wide (Freund et al. 1985). Versus cells in L4 and the infragranular layer receive thalamocortical projections converging from a region of Ts with a diameter of 4 elements. Thalamocortical projections account for about 8% of all connections received by layer IV neurons, consistent with anatomical estimates (Ahmed et al. 1994; Latawiec et al. 2000; Peters and Payne 1993). Corticothalamic axons descend from the infragranular excitatory cells into their corresponding thalamic relay sectors, contacting all cell types present in these structures, consistent with anatomical data (Montero 1991; Robson 1983; Weber et al. 1983). En route, such fibers send collaterals to the RT nucleus. Consistent with experimental observations (Golshani et al. 2001), corticoreticular projections are substantially stronger (2.5×) than corticothalamic projections. The topography of corticothalamic connectivity matches that of the thalamocortical connectivity (Jones 2002).

Transmission delays

Transmission of signals within and across cortical areas occurs through several successive stages, including axonal conduction, synaptic delays, and postsynaptic potential (PSP) generation. Each of these stages is associated with delays in the transmission of a signal. Measured latencies between the firing of successive visual cortical areas in the cat have been estimated to lie between 5 and 15 ms (Dinse and Kruger 1994) in the forward direction. Geniculocortical latencies may be even shorter (Bullier and Henry 1979). Backward connections may be slower conducting. For instance, latencies from areas 18 and 19 to area 17 are 6 and 10 ms, respectively (Bullier et al. 1988).

Because of the fact that the simulated cortices contain only 3 layers (instead of 6), we account for experimentally measured latencies along polysynaptic pathways by assuming comparatively longer transmission delays along certain pathways. Transmission delays for individual connections are sampled from Gaussian distributions with a SD of 1 ms. Each set of connections in the model is associated with a specific mean delay. Mean conduction delays are set to 2 ms for intralaminar connections and for most interlaminar connections. Infragranular to layer 4 connections are delayed on average by 7 ms, to account for disynaptic transmission through layers 5 and 6. Thalamocortical connections and forward connections from Vp to Vs have a mean delay of 3 ms, whereas corticothalamic connections and backward connections from Vs to Vp have a mean delay of 8 ms, again taking into account a disynaptic pathway through layers 5 and 6.

Model neurons

Both excitatory and inhibitory neurons are modeled as single-compartment spiking neurons incorporating Hodgkin–Huxley style currents. To model the contributions of key intrinsic currents, while preserving the computational efficiency of integrate-and-fire neurons that is necessary when computing a large-scale network, we devised a simplification of the fast-spiking currents (I_{Na} and I_K). Model neurons thus behave like a hybrid between traditional integrate-and-fire neurons and full-fledged Hodgkin–Huxley neurons.

A dynamic threshold (θ) is defined for each cell that determines at which membrane potential the cell should fire

$$\frac{d\theta}{dt} = -(\theta - \theta_{eq})/\tau_\theta$$

The resting threshold (θ_{eq}) determines the equilibrium threshold potential for both excitatory and inhibitory neurons. The threshold time constant τ_θ determines the time to return to the equilibrium threshold. The specific values were chosen to match absolute refractory periods for different neuron types (Table 2).

The change in membrane potential V for each neuron is as follows

$$\frac{dV}{dt} = [-g_{NaL}(V - E_{Na}) - g_{KL}(V - E_K) - I_{syn} - I_{int}]/\tau_m - g_{spike}(V - E_K)/\tau_{spike}$$

where the conductances for the sodium leak ($g_{NaL} = 0.2$) and potassium leak ($g_{KL} = 1.0$ –1.85) are the primary determinants of the resting membrane potential. Conductance units are dimensionless because of the fact that the neurons do not have a defined area or volume.

When the membrane potential V exceeds the threshold θ , a spike is generated by setting both V and θ instantaneously to the sodium reversal potential ($E_{Na} = 30$ mV), modeling the contribution of the fast-spiking I_{Na} current. The activation of a fast potassium current during a spike is represented by a brief pulse (duration t_{spike} , Table 2) with an amplitude of $g_{spike} = 1$, thereby driving the membrane potential toward the potassium reversal potential ($E_K = -90$ mV), while continuing to integrate intrinsic and synaptic currents. The

TABLE 2. *Neuron spike parameters*

Neuron Type	θ_{eq} , mV	τ_θ , ms	t_{spike} , ms	τ_{spike} , ms	τ_m , ms
Cortical Exc	-51.0	2.0	2.0	1.75	16.0
Cortical Inh	-53.0	1.0	1.0	0.5	8.0
Thalamic	-53.0	0.75	1.0	0.75	8.0

integration of the fast hyperpolarizing current occurs faster than the membrane potential and is therefore governed by a “spike” time constant ($\tau_{\text{spike}} \leq \tau_m$). The cell is unable to fire until $\theta \leq V$. With these three parameters, τ_θ , τ_{spike} , and t_{spike} , we model key characteristics of spike generation including action potential width, afterhyperpolarization, and relative refractory period (Table 2).

The membrane time constants τ_m are consistent with experimental data (Baranyi et al. 1993; Connors et al. 1982; Kim and Connors 1993; Mason et al. 1991).

Two main categories of input currents contribute to the membrane potential, synaptic input (I_{syn}) and intrinsic currents (I_{int}), which are described below.

Synaptic channels

The synaptic input I_{syn} is the sum of all synaptic channel currents, $I_{\text{syn}} = \sum_{ij} g_j^{(i)}(V - E_j)$. Simulated synaptic channels provide voltage-dependent (NMDA-like) and voltage-independent (AMPA-like) excitation, as well as fast (GABA_A -like) and slow (GABA_B -like) inhibition. The conductance for each afferent i , on each channel j , specifies the amplitude and time course of the PSPs. The reversal potential for each channel E_j determines whether a current is inhibitory or excitatory. Electrical couplings between cortical inhibitory populations have been observed experimentally (Galarreta and Hestrin 1999) but are not modeled here.

Synaptic activation is expressed as the change of a channel conductance, $g(t)$, according to a dual-exponential response to single spike events, given by

$$g(t) = g_{\text{peak}} \frac{e^{-t/\tau_1} - e^{-t/\tau_2}}{e^{-t_{\text{peak}}/\tau_1} - e^{-t_{\text{peak}}/\tau_2}}$$

where τ_1 and τ_2 are the parameterizing the rise and decay time constants, respectively, and t_{peak} is the time to peak

$$t_{\text{peak}} = \frac{\tau_2 \tau_1}{\tau_2 - \tau_1} \ln \left(\frac{\tau_2}{\tau_1} \right)$$

Conductances are implicitly normalized by a leak membrane conductance and are adimensional. The time constants and reversal potential for each channel type were taken from the neurophysiological literature (Otis and Mody 1992; Otis et al. 1993; Stern et al. 1992). The peak conductances g_{peak} were chosen to conform to a few simple constraints that led to regular network behavior. These constraints consisted of having: 1) peak excitatory postsynaptic potentials (EPSPs) of 1 mV in AMPA-like channels; 2) matched integrated excitatory postsynaptic currents (EPSCs) through AMPA and unblocked NMDA channels; 3) matched integrated inhibitory postsynaptic currents (IPSCs) through GABA_A and GABA_B channels. The activation of NMDA-like channels was expressed as

$$\tilde{g}_{\text{NMDA}} = m(V)g_{\text{NMDA}}(t),$$

where $g_{\text{NMDA}}(t)$ is a dual-exponential impulse response and $m(V)$ is a sum of 2 exponentials functions with fast and slow time constants, which modulates the change in the NMDA conductance. This modulation mimics the voltage-dependent affinity of the Mg^{2+} located inside the channel pore. Additionally, although the blocking of NMDA channels by Mg^{2+} occurs instantaneously (<0.06 μ s) there is a slower dynamic to the unblocking process occurring on 2 timescales, as recently described (Vargas-Caballero and Robinson 2003). Based on this work, we model a 2-stage unblocking process with one component that unblocks quickly (about 1 ms) and a second slow component that unblocks in about 20 ms. Specific parameter settings for the different type of synaptic channels are listed in Table 3.

AMPA-like channels are used for most excitatory connections implemented in the model. For horizontal connections in supragranular layers, vertical projections from supragranular to infragranular

TABLE 3. Synaptic channel parameters

Receptor	g_{peak}	τ_1 , ms	τ_2 , ms	E_{rev} , mV
AMPA	0.1	0.5	2.4	0
GABA_A	0.33	1	7	-70
GABA_A TC	0.33	1	7	-80
GABA_B	0.0132	60	200	-90
NMDA	0.075	4	40	0

layers, as well as for backward connections from Versus to supragranular cells of Vp, we add model voltage-dependent NMDA-like channels. This choice enabled these connections to modulate the firing of target units without disrupting their response selectivity. Evidence supporting this choice includes the finding that voltage-gated NMDA receptors are denser in the supragranular layers of visual cortex (Fox et al. 1989; Rosier et al. 1993); in addition, the effectiveness of these connections seems in part contingent on a concomitant depolarization of target cells that are not in visuotopic register with the sources of afferentation (Bullier et al. 1988; Hirsch and Gilbert 1991; Salin and Bullier 1995).

Inhibition in the thalamus was mediated by fast (GABA_A -like) synapses. Because of nucleus specific differences in the chloride reversal potential, reticulothalamic GABA_A (TC) channels had a reversal potential more negative for thalamic relay cells (about -80 mV) than for cells found in the reticular nucleus (about -70 mV) (Ulrich and Huguenard 1997).

Synaptic depression

There is substantial evidence that the rapid plasticity of excitatory and inhibitory synaptic responses is dominated by short-term depression and caused by the depletion of presynaptic pools of readily releasable neurotransmitter vesicles (Zucker and Regehr 2002). In the model, short-term depression of both excitatory and inhibitory connections was based on a simple vesicle pool model (Abbott et al. 1997; Galarreta and Hestrin 1998; Tsodyks and Markram 1997). Synaptic depression was modeled by scaling the peak conductance of a given synaptic channel by the size of the corresponding presynaptic pool of synaptic “vesicles.” The dynamics of this pool was governed by the simple first-order equation $dP/dt = -\text{spike} \cdot \delta_p \cdot P + (P_{\text{peak}} - P)/\tau_p$. The pool P decreases by the fraction δ_p for each spike = 1. The pool recovers its peak value P_{peak} according to the time constant τ_p .

Intrinsic ion channel properties of thalamic and cortical neurons

Ion channel currents that influence intrinsic firing properties of thalamic and cortical neurons were modeled according to the Hodgkin-Huxley formalism $I_{\text{int}} = g_{\text{peak}} m^N h(V - E_{\text{int}})$, where g_{peak} is the maximal conductance for the channel, m and h determine the activation and inactivation respectively (see following text), and E_{int} is the reversal potential for the given channel. The factor N allows the activation to occur on a different order than inactivation. The gating of activation and inactivation follows the same first-order kinetics equation: $dx/dt = [x_\infty(V) - x]/\tau_x(V)$ where x_∞ is the steady-state activation/inactivation value for the channel.

PACEMAKER CURRENT I_h . I_h is a noninactivating hyperpolarization-activated cation current that is believed to underlie a depolarizing “pacemaker” potential observed in many cells throughout the brain, including the thalamus and the cortex (Huguenard and McCormick 1992; McCormick and Bal 1997; Robinson and Siegelbaum 2003). The activation variable m_h for I_h is modeled by $m_h = 1/[1 + \exp((V - V_{\text{threshold}})/5.5)]$, with $V_{\text{threshold}} = -75.0$. The rate τ_m of activation and deactivation also follows Huguenard and McCormick (1992): $\tau_m = 1/[\exp(-14.59 - 0.086V) + \exp(-1.87 + 0.0701V)]$.

Only thalamic (Tp and Ts) and intrinsically bursting cells (IB: 30% of excitatory cells in L5–6) were endowed with I_h channels. The highest density of I_h channels in cortex is expressed in the dendrites of layer V neurons and was therefore included in L5–6 neurons (Robinson and Siegelbaum 2003).

LOW-THRESHOLD CALCIUM CURRENT I_T . I_T is a low-threshold fast-activating calcium current that underlies the generation of bursts in the thalamus and reticular nucleus (Huguenard and Prince 1992; McCormick and Bal 1997). We use the formulation of I_T from previous modeling work (Destexhe et al. 1996a; Huguenard and McCormick 1992). Using the steady-state activation formulae, the activation variable is given by $m_\infty = 1/\{1 + \exp[-(V + 59.0)/6.2]\}$, with the voltage-dependent time constant $\tau_m = \{0.22/\exp[-(V + 132.0)/16.7]\} + \exp[(V + 16.8)/18.2] + 0.13$. Inactivation of I_T is defined as $h_\infty = 1/\{1 + \exp[(V + 83.0)/4.0]\}$ with the inactivation time constant $\tau_h = \{8.2 + \{56.6 + 0.27 \exp[(V + 115.2)/5.0]\}\}/\{1.0 + \exp[(V + 86.0)/3.2]\}$. Only thalamic (Tp and Ts) and reticular (Rp and Rs) cells incorporated I_T channels. This current combined with I_h (described above) endowed thalamic relay cells with intrinsic bursting properties. Although some cortical neurons contain T-type currents (Paré and Lang 1998), we did not include them in model cortical neurons for the purpose of the present simulations. A slower T-current is known to exist in reticular neurons (Destexhe et al. 1996b), but was not modeled here, although it is not expected that this current would have a significant impact on the present results.

PERSISTENT SODIUM CURRENT $I_{Na(p)}$. This sodium current is found in virtually all cortical neurons (French et al. 1990; Kay et al. 1998; Mittmann and Alzheimer 1998; Stafstrom et al. 1984). It activates quickly near the resting potential and is considered persistent because it inactivates very slowly (on the order of seconds). We borrowed the formulation for $I_{Na(p)}$ from previous work (Compte et al. 2003; Fleidervish et al. 1996). The steady-state values for activation are used because they are considered to be instantaneous given their rapid time course (<1 ms). The steady-state activation is $m_\infty(V) = 1/[1 + \exp(-V + 55.7)/7.7]$. We did not model the inactivation of this current given its very slow time course. All cells in the model contained $I_{Na(p)}$.

DEPOLARIZATION-ACTIVATED POTASSIUM CURRENT I_{DK} . A Na^+ - or Ca^{2+} -activated K^+ current appears to play an important role in the termination of the depolarized phase of the slow oscillation (Sanchez-Vives and McCormick 2000; Steriade et al. 2001). Both Na^+ and Ca^{2+} currents are activated by the influx of ions that build up during periods of depolarization or spiking. To reduce the computational burden, we did not explicitly model either Ca^{2+} influx during spiking or the intracellular Na^+ concentration. These concentrations increase most when the membrane potential is elevated. Therefore we chose to model this current as a generic activity-dependent potassium current with some activation properties taken from models of I_{KNa} (Wang and Lambert 2003). To characterize this depolarization-dependent influx, we use a sigmoid threshold function to determine how much the measure of depolarization D should increase for the current membrane potential. The factor D accumulates with depolarization and decays to the internal equilibrium concentration according to $dD/dt = D_{influx} - D \cdot (1 - D_{eq})/\tau_D$ where $D_{influx} = 1/[1 + \exp[-(V - D_0)/\sigma_D]]$. The voltage-dependent influx D_{influx} is determined by a sigmoid function with a threshold $D_0 = -10$ mV and slope $\sigma_D = 5.0$. The equilibrium level for the depolarization-dependent value is $D_{eq} = 0.001$, and $\tau_D = 1.25$ s is the time constant that determines the return to D_{eq} . The depolarization-dependent activation of the current I_{DK} is given by $m_\infty = 1/1 + (d_{1/2}D)^{3.5}$. The parameter $d_{1/2} = 0.25$ determines the level of D necessary for half activation. All cortical (L5–6, L4, and L2–3; excitatory and inhibitory) cells contained I_{DK} channels.

INFLUENCE OF DIFFUSE NEUROMODULATORY SYSTEMS. Under physiological conditions, ascending neuromodulatory projections

modulate the mode of firing in the thalamocortical system. Ascending neuromodulatory projections from several brain stem nuclei and the basal forebrain activate muscarinic, noradrenergic, serotonergic, histaminergic, and glutamate metabotropic receptors, which modulate various cellular conductances that influence the overall level of depolarization on which the sleep–wake cycle critically depends (McCormick 1992). As will be specified in the RESULTS, the various actions of neuromodulators are modeled as simultaneous changes of the conductances for I_{KL} , I_h , I_{DK} , $I_{Na(p)}$, and AMPA synapses of the cortex, thalamus, and reticular nucleus.

SPONTANEOUS ACTIVITY: OPTIC NERVE FIRING AND MINIS. The primary source of noise in the model was random spontaneous optic tract firing (45 spikes/s) modeled as 1,600 separate Poisson processes, which were independent of the behavioral state (Mukhametov et al. 1970). The simulated optic nerve cells connect to Tp by diffuse projections with independent Gaussian latencies on each connection. This decreases the degree of synchronicity of spontaneous input and produces the slightly overlapping receptive fields observed in the LGN (Kara and Reid 2003). This random activity percolated throughout the network, producing irregular spontaneous activity in all layers of the model.

In addition, we modeled “minis,” the spontaneous release of neurotransmitter quanta (Vautrin and Barker 2003), as low-amplitude PSPs (mean = 0.5 ± 0.25 mV) consistent with experimental observations (Timofeev et al. 2000). The mean frequency of these Poisson distributed synaptic minis was set to 2 Hz (total for an individual cell).

Data recording

All state variables of the network (V_m , intrinsic and synaptic conductances and currents) were recorded during each simulation. These recordings were then used to visualize the model activity in a way that allowed comparison with experimental data—including local field potentials, optical dye recordings, and intrinsic and synaptic channel conductances.

The local field potential (LFP) as recorded *in vivo* is thought to be primarily a reflection of the net synaptic activity (i.e., not the mean firing rate) within a local region (several millimeters) around the measuring electrode (Logothetis et al. 2001). A signal meant to resemble the local field potential was calculated as a spatial average of membrane potentials, $LFP = 1 - 1/N \sum_{i=1}^N V_i$, for all cells i within a given radius (unless otherwise specified, the radius = 20 units = the area of an entire model layer).

Voltage-sensitive optical dye recordings provide a technique to visualize spatiotemporal activity patterns in large-scale populations on a rapid timescale (about 10 ms) (Fitzpatrick 2000). Accordingly, we visualized large-scale activity patterns by displaying average membrane potential (10 ms) while preserving topographic relationships between neurons.

Conductances of individual channels can be measured experimentally using patch-clamp techniques. In the model, all conductances are explicitly calculated, and therefore easily recorded under all conditions.

Simulation techniques

SYNTHESIS. All simulations were performed using a general-purpose object-oriented interactive neural simulator called *Synthesis* written by S. Hill (www.infinitedegrees.info). *Synthesis* provides a complete simulation environment, including: a computation server capable of parallel and distributed computation, a graphical user-interface for interactive visualization and manipulation, a scripting language for automating parameter searches and experiments, an interactive command-line environment for controlling the simulation, data agents for data gathering and analysis, and a library of standard

neuron, synapse, and connection pattern models. The simulation server is multithreaded for multiprocessor computation and capable of distributing a simulation across multiple networked computers. *Synthesis* allows the user to interact fully with a simulation, visualizing and recording all variables—at different levels and timescales—while observing all network interactions and controlling all parameters in real time throughout the course of a simulation.

NUMERICAL METHODS. Differential equations were numerically integrated using the Runge–Kutta 4th-order method (Press et al. 1992) with a step size of 0.25 ms. The model was tested at smaller time steps with no significant differences observed. The generation of optic nerve activity and probabilistic connectivity patterns were based on standard pseudorandom number generator routines (Press et al. 1992). Analysis of the simulation data was carried out using standard toolboxes in MATLAB (The MathWorks, Natick, MA).

COMPUTATIONAL TIME. The simulations were carried out on dual-processor 2.0 Ghz Power Macintosh G5 machines running Mac OS 10.3 and equipped with 3.5 GB RAM (Apple, Cupertino, CA). Each simulation of the full model used approximately 1.7 GB RAM. Computational performance varied with the mean firing rate and ranged from 500 to 700 ms/h for the full model. A single simulation run of 3 s in duration required over 5 h to compute.

RESULTS

The overall organization of the model thalamocortical system is shown in Fig. 1. We chose to model the thalamocortical system of the cat because most intracellular recordings during the slow oscillation have been obtained from this system (Steriade 2003). The full model contains 65,400 spiking neurons with 4,860,450 connections organized in regions and pathways, consisting of a primary and a secondary area of visual cortex (Vp and Vs), 2 corresponding regions of the dorsal thalamus (Tp and Ts), and 2 regions of the reticular thalamic nucleus (Rp and Rs). Vp represents a restricted portion of area 17 in the cat (i.e., about 1 cm²) and it contains units with small receptive fields that are selective for oriented segments. Versus represents a corresponding part of an extrastriate area with coarser topography, containing units with larger receptive fields that are selective for oriented lines and for line crossings. Tp and Ts correspond to a portion of the lateral geniculate nucleus (LGN) and to a portion of the lateral posterior pulvinar complex (LP), respectively. The thalamocortical model builds on a previously published architecture that was used to explore properties of synchrony and spike timing in response to visual stimuli and that successfully reproduced several experimental results (Lumer et al. 1997a,b).

A central feature of the model is the subdivision of the simulated cortex into 3 layers with different patterns of afferent, efferent, and local connectivity corresponding to supragranular layers, infragranular layers, and layer 4 (Figs. 1 and 2). Another key feature is the detailed simulation of horizontal intralaminar connections, vertical interlaminar connections within Vp and Vs, forward and backward connections between Vp and Vs, thalamocortical and corticothalamic connections, and connections from thalamic relay nuclei and cortex to the nucleus reticularis. We believe all these features constitute the minimum necessary components of a prototypical thalamocortical system.

Individual cortical and thalamic neurons, both excitatory and inhibitory, were modeled as single-compartment integrate-and-fire units using cellular constants from regular- and fast-spiking

neurons, respectively (Connors et al. 1982). Intrinsic currents were modeled using details of intracellular channel dynamics including those regulating hyperpolarization-activated cations I_{h} , low-threshold calcium I_T , persistent sodium $I_{Na(p)}$, potassium leak I_{KL} , and a depolarization-dependent potassium current I_{DK} . Synaptic interactions occurred through simulated channels that provided voltage-dependent (NMDA-like) and voltage-independent (AMPA-like) excitation, as well as fast ($GABA_A$ -like) and slow ($GABA_B$ -like) inhibition. All connections were endowed with conduction delays. Finally, neuromodulatory influences, such as those attributed to acetylcholine, were modeled as diffuse changes of intrinsic and synaptic conductances.

In what follows, we first show that our large-scale model of the thalamocortical system reproduces various aspects of spontaneous activity during wakefulness including low-voltage fast activity in the EEG, irregular firing, correlated subthreshold activity that reflects the functional architecture, and selective response to stimuli including gamma frequency synchronization in the evoked response. We then show that the model transitions to slow-wave sleep primarily arise from an increase in the potassium leak (I_{KL}) current. The slow oscillation that subsequently emerges has many properties that are consistent with experimental results including a bimodal membrane potential distribution, a disfacilitated and silent down-state and a depolarized, high-conductance up-state that exhibits gamma frequency synchronization and mean firing rates in the range of 10–20 Hz. By performing several manipulations on the key model parameters, we investigate which intrinsic and synaptic currents underlie the initiation, maintenance, and termination of the slow oscillation. Finally, we demonstrate that the synchronization of the slow oscillation in the model is dependent on corticocortical connections, consistent with experimental observations.

The robustness of the results presented here was tested by replicating the experiments described below while systematically varying the relevant parameters as well as by starting from different initial conditions (the precise location of connections are generated probabilistically; see METHODS). For all simulation results described below, small perturbations in parameter values did not significantly alter the results (actual results of robustness tests are not shown because of the extremely large size of parameter space explored, amounting to more than 3 years of CPU time).

In the waking mode, the model exhibits spontaneous activity throughout the cortex and shows selective responses to visual stimuli

In the waking mode, spontaneous activity originating in retinothalamic afferents spreads throughout the thalamocortical system (Fig. 3, *A–D, left*). When a visual stimulus is applied, a selective response emerges from the spontaneous activity and high-frequency firing occurs for the duration of the stimulus (Fig. 3, *A–D, right*).

Figure 3*A* depicts the spatiotemporal organization of the membrane potential for 25 neurons for each of the 3 layers of Vp and the corresponding sectors of Tp and Rp. During the spontaneous condition (Fig. 3*A*, *left*), the membrane potential rapidly fluctuates around approximately 60 mV. The cells are rarely hyperpolarized below –70 mV. Occasionally, neurons

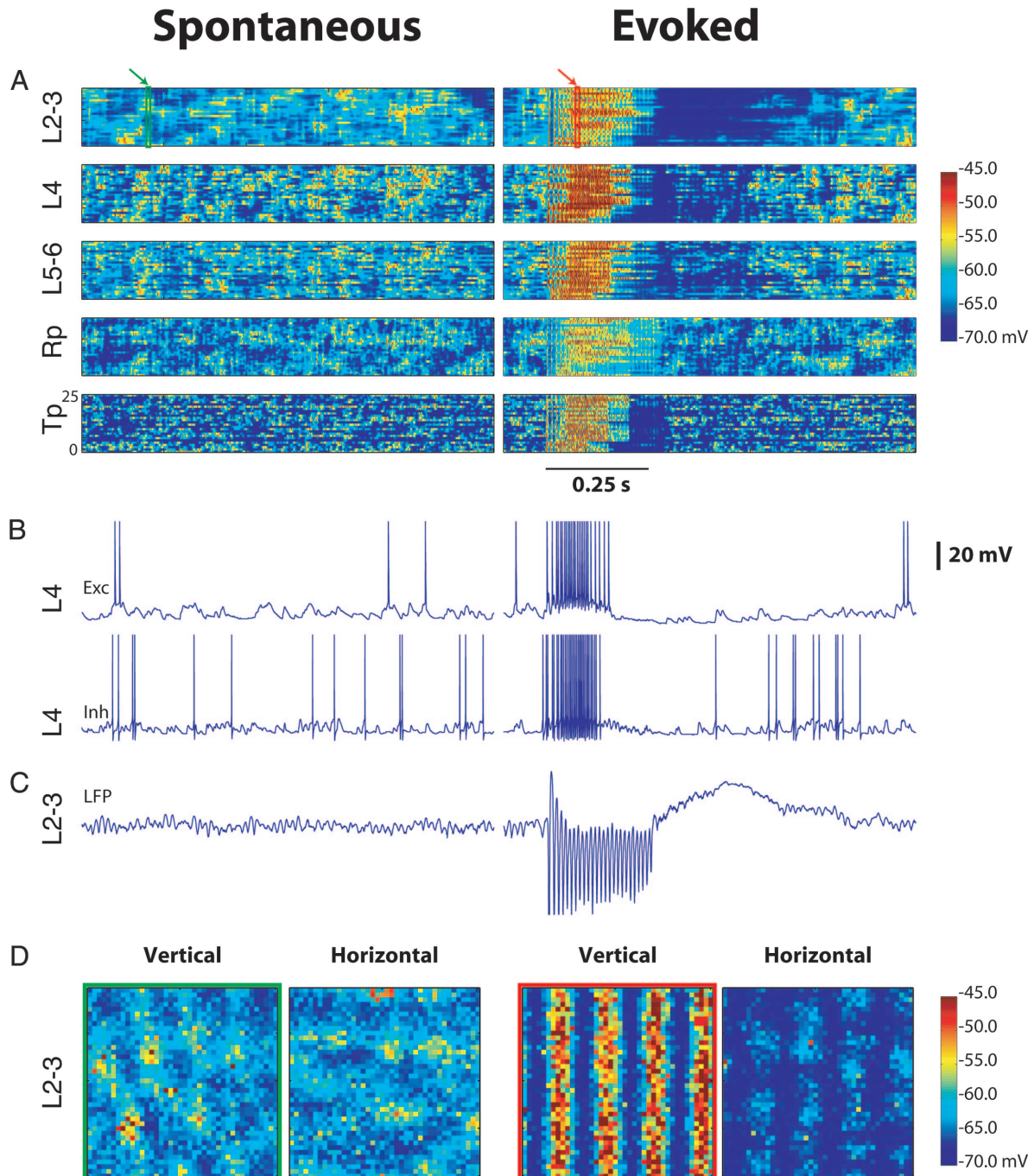


FIG. 3. Spontaneous and evoked activity in the thalamocortical network during the waking mode. *Left side:* spontaneous activity. *Right side:* evoked activity arising from a stimulus presentation (vertical moving grating stimulus at 2 cycles/s). *A:* membrane potential rasters displaying activity over 1 s for 25 neighboring neurons. Note irregular firing and membrane potential fluctuations in individual cells and throughout all layers during spontaneous activity. During the evoked response, notice the strong depolarization and intense firing of individual cells and the strong synchronized oscillations occurring throughout all layers of the network. *B:* intracellular potentials for representative excitatory and inhibitory neurons in L4. Note the low level of spontaneous firing that becomes significantly elevated during the stimulus presentation. *C:* local field potential (LFP) computed from average synaptic input in L2–3. Note the strong gamma frequency oscillations during the stimulus presentation. *D:* time-averaged topographic representation of the membrane potential for 2 orientation selective populations in L2–3 of Vp during spontaneous and evoked conditions. Note that the orientation preference is visible in the average spontaneous activity. Vertically selective population responds preferentially to the vertical grating, whereas the horizontally selective population is silenced. Green box and red boxes in *A* indicate the time windows (10 ms) used for the average spontaneous and evoked activity, respectively.

become depolarized enough to spike and irregular firing occurs in all layers. L4 is slightly more depolarized than other cortical layers because of the high level of synaptic input from Tp.

A moving visual stimulus, consisting of a 2-dimensional vertically oriented grating, was presented by firing a patterned

subset of neurons in the optic tract for a duration of 250 ms. During the stimulus presentation, the vertically selective cells display a dramatically increased firing rate (10×) and high-frequency synchronized oscillations are clearly observable in the membrane potential (Fig. 3*A*, *right*). Poststimulus offset

responses consist of marked inhibition and decreased firing, while the network reconfigures and resumes generating spontaneous activity after a few dozen milliseconds.

Intracellular unit recordings (Fig. 3B) depict spontaneous and evoked activity comparable to intracellular recording *in vivo*. Specifically, cortical excitatory and inhibitory neurons fire irregularly at low rates (2–10 Hz) during spontaneous activity, while firing at elevated rates (20–100 Hz) during stimulation, consistent with experimental data (Azouz and Gray 1999). In these traces, the evoked activity appears to end prematurely because the stimulus is a slowly drifting grating and therefore does not rest within the receptive field of the individual cells shown for the entire time period.

The LFP (see METHODS), reflecting spontaneous and evoked activity, shows low-voltage fast-activity patterns in the absence of stimuli (Fig. 3C, *left*) and clear evoked responses with high-frequency oscillations during stimulus presentation (Fig. 3C, *right*), consistent with LFPs recorded *in vivo* during stimulation (Gray and Singer 1989).

The topographic displays (Fig. 3D) show time-averaged (10 ms) membrane potentials in L2–3. Spontaneous activity in the model has a subthreshold correlational structure that reflects the orientation preference of the neural population (Fig. 3D, *left*). Specifically, subthreshold vertical and horizontal bars of depolarization are visible in the average membrane potential for each selective population even when no stimulus is applied. The spontaneous emergence of correlated activity reflects the underlying orientation-selective mechanisms, consistent with optical dye recordings in the monkey showing that cellular membrane potential fluctuations during spontaneous activity reflect the functional architecture and selective response mechanisms of visual cortex (Kenet et al. 2003; Tsodyks et al. 1999). When a vertical grating is presented, vertically selective cells respond preferentially, whereas cells selective for horizontal features remain virtually silent, as is evident in Fig. 3D (*right*). A movie of the topographic view of several layers throughout the model network during both spontaneous activity and during stimulus presentation is available (see supplementary video #1¹).

An increase in potassium leak conductance triggers the transition from the waking mode to the sleep mode

In the model, the transition from the waking mode to the sleep mode (Fig. 4) comes about primarily by increasing the potassium leak conductance g_{KL} (from 1.0 to 1.85), which is present in all model neurons. This corresponds to the unblocking of background potassium leak channels arising from the

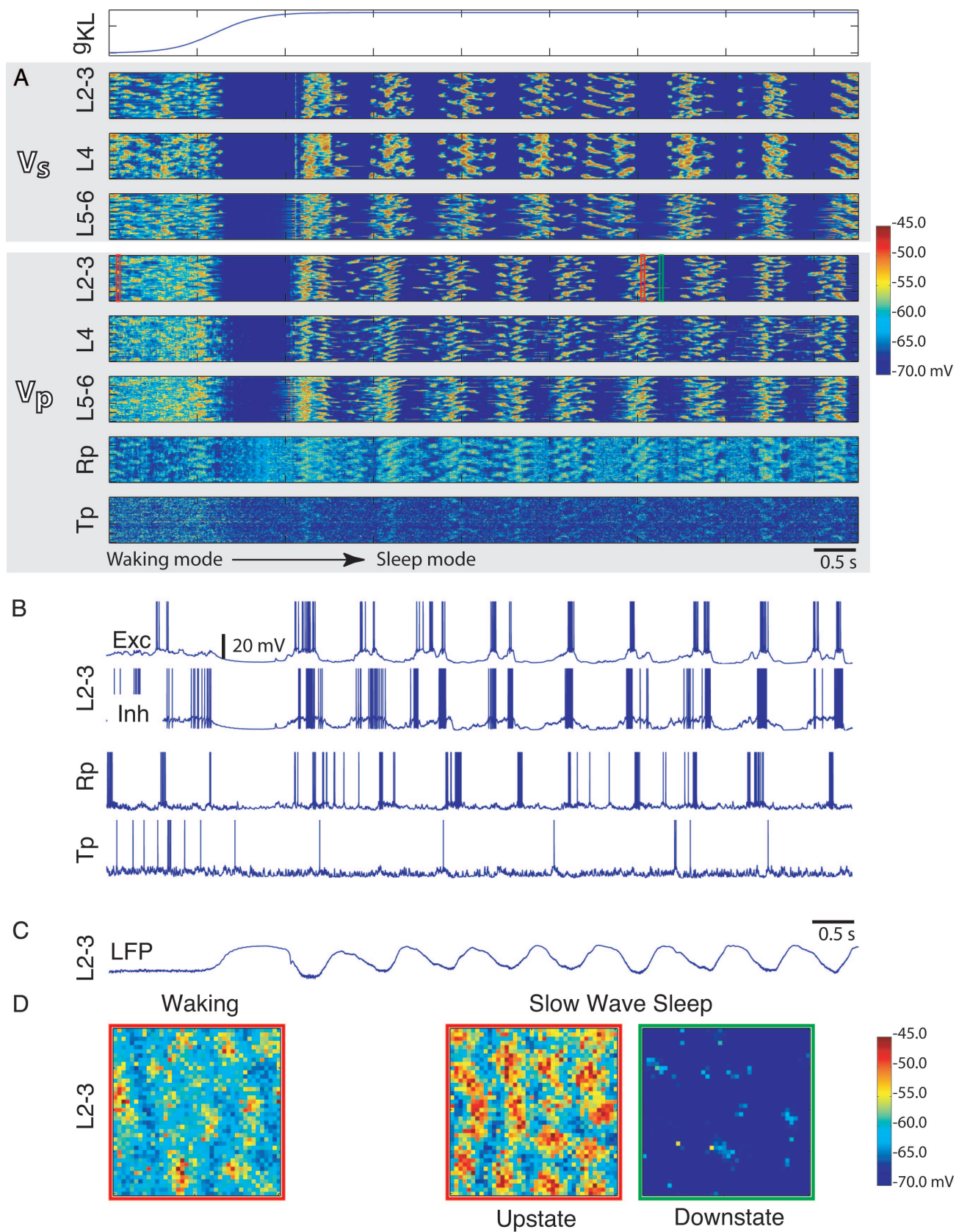
reduced actions during sleep of neuromodulators such as acetylcholine (McCormick 1992). Without this single change of g_{KL} , the network does not enter the hyperpolarized, silent state necessary for the sleep mode. A number of other network parameters are modulated during the transition from wakefulness to sleep. Several studies suggest that muscarinic receptor activation can significantly inhibit the $I_{Na(p)}$ conductance (Mittmann and Alzheimer 1998). The removal of acetylcholine would therefore cause an effective increase in the conductance of $I_{Na(p)}$ throughout the network. We model this by increasing the conductance $g_{Na(p)}$ for the sleep mode (from 0.5 to 1.25). Acetylcholine has also been shown to shift the activation curve of I_h to more depolarized levels (McCormick et al. 1993). We model this by increasing the conductance of I_h during the sleep mode (from 1.0 to 2.0). I_T is also known to be inhibited by activation of muscarinic receptors (McCormick 1992). We model this by increasing the peak conductance of I_T from wakefulness to sleep (from 1.0 to 1.25). Neither of the changes to I_h or I_T played a significant role in the transition to sleep. The removal of acetylcholine and norepinephrine unblocks slow potassium currents (McCormick 1992), which are represented in the model by the depolarization-activated potassium current I_{DK} . We increased g_{DK} (from 0.5 to 1.25) in parallel with g_{KL} . Finally, muscarinic receptor activation reduces intracortical EPSPs (Gil et al. 1997), suggesting that—during wakefulness—excitatory synapses are depressed relative to slow-wave sleep. We model this change by increasing the amplitude of AMPA EPSPs (by 50%) from the waking mode to the sleep mode.

Membrane potential rasters for a population of neighboring cells from throughout both Vp and Versus of the network illustrate the result of this modulation (Fig. 4A). Spontaneous activity during the waking mode gradually diminishes and the entire network enters a silent down-state by the time g_{KL} has reached its maximum. After several hundred milliseconds of silence, the network begins to depolarize as a result of the activation of $I_{Na(p)}$ and rapidly enters an up-state with depolarized membrane potential, elevated firing, and apparent synchronization throughout the network. In the sleep mode, the thalamus is quieted, although it becomes periodically depolarized, producing short spike bursts in response to cortical depolarization. Vp and Versus fall in and out of phase initially, but gradually become and remain synchronized. Intracellular activity in Versus is similar to that shown in Vp, although it tends to have less noisy down-states because of the lack of optic nerve input.

Figure 4B shows the same transition from the irregular firing of the waking mode to the sleep mode in 2 neighboring excitatory and inhibitory cells in L2–3 as well as single cells in the model thalamus and reticular nucleus. It is evident that the

¹ The Supplementary Material for this article (two movies) is available online at <http://jn.physiology.org/cgi/content/full/00915.2004/DC1>.

FIG. 4. Transition from the waking mode to the sleep mode. Entire cortical network undergoes a dramatic change at many different levels as the potassium leak conductance (g_{KL}) increases. A–D are aligned on the same timescale. A: membrane potential rasters of the membrane potentials of 100 neighboring cells within cortical areas Versus and Vp over 8.5 s. B: individual intracellular traces from excitatory and inhibitory cells, revealing the emergence of the slow oscillation with up- and down-states. Rp and Tp cells also reflect the cortical slow oscillation. C: LFP reflects population synchronization at the frequency of the slow oscillation (<1 Hz). Note that the negative deflection corresponds to the depolarized phase of the slow oscillation. D: topographical activity plots show the average membrane potential during wakefulness (green), and the up- and down-states of the slow oscillation in the sleep mode. Red and green boxes (in A) during the waking mode and the sleep mode indicate the time window (10 ms) of the averaged activity. Note that the membrane potential of all cells in the network becomes hyperpolarized as g_{KL} increases and the network becomes silent. After several hundred milliseconds, individual cells become depolarized and fire for several hundred milliseconds, during which the entire cortical network becomes strongly engaged in the up-state. LFP reflects the synchronization of the network activity showing the transition from low-voltage fast activity to high-amplitude slow activity. Notice the increased level of activity during the up-state compared with the down-state as well as to the waking mode.



cortical cells undergo up- and down-states almost simultaneously. The reflection of slow oscillation activity is also seen in cells located in both Tp and Rp. The intracellular traces of

these cells are comparable to those recorded *in vivo* (Fuen-tealba et al. 2004; Steriade et al. 2001; Timofeev and Steriade 1996).

As revealed by the LFP (Fig. 4C), when the network transitions from the waking mode to the sleep mode, the population activity changes from irregular activity (low-voltage fast activity) to a synchronized oscillation that continues indefinitely (high-voltage slow activity).

Figure 4D depicts a topographic map of average membrane potentials (10 ms) from L2–3 during periods of the waking mode and during up- and down-states during the sleep mode. The topographic map during waking (Fig. 4D, left) is similar to that shown in Fig. 3D. The 2 topographical maps taken from the sleep mode illustrate the dramatic difference between up- and down-states. The up-state is clearly more depolarized than the down-state and neurons are intensely active. During the down state, neurons are hyperpolarized and virtually silent (Fig. 4D, right). The rapid development of this synchronization in the network is consistent with observations of the transition from wakefulness to natural sleep in cats (Steriade et al. 2001). A movie of the topographic view of several layers throughout the model starting from the waking mode and showing the transition to the sleep mode is available (see supplementary video #2).

Additional simulations (not shown) reveal that when the network is transitioned more gradually from the waking mode to the sleep mode, and when the parameters influenced by neuromodulators are at an intermediate level, it exhibits sleep spindles. Spindle activity will be the object of a future publication and will not be discussed here.

In the sleep mode, the model displays a stable slow oscillation consisting of an up-state and a down-state

In the sleep mode, the network oscillates between a depolarized and hyperpolarized phase in a synchronized fashion (Fig. 5). The depolarized “up-state” lasts about 300–600 ms and is characterized by an average membrane potential of around -58 mV, elevated firing rates, and elevated intrinsic and synaptic currents. The hyperpolarized “down-state” lasts between 400 and 600 ms and is characterized by an average membrane potential of around -75 mV, an absence of firing, and very low intrinsic and synaptic currents. The LFP (Fig. 5, top) depicts the population level synchronization. Membrane potential rasters depict activity for each layer showing the synchronization of the up- and down-states across all layers and all neurons of the model cortex (Fig. 5, rasters). The network produces regular alternations between up- and down-states at about 1 Hz. Intracellular traces reflect the irregularity and variety of up- and down-states typical of the slow oscillation (Fig. 5, A–C, intracellular traces).

If the transition from the waking mode to the sleep mode is more gradual, the slow oscillations produced by the network occur at more irregular intervals and are less tightly synchronous (not shown). Regions of the network initiate the up-state of the oscillation and gradually recruit the rest of the network after several cycles. In general, the synchronization of the oscillation is very dynamic, with each new cycle dependent on the activity during the previous oscillation. For instance, when an up-state spontaneously produces high firing rates across the network, several subsequent cycles are increasingly synchronized. As the system relaxes, the next cycles of the oscillation become less tightly synchronized. The duration of the up- and down-states under such circumstances are more variable,

closely resembling the intracellular traces recorded during natural sleep (Steriade et al. 2001). For the purposes of this paper we have focused on the prototypical slow oscillation with clearly defined up- and down-states similar to those recorded during deeper stages of natural sleep (Amzica and Steriade 1998) or under ketamine–xylazine anesthesia (Steriade et al. 1993).

The slow oscillation propagates through intra- and interareal connections

The model slow oscillation propagates at different spatial and temporal scales. First, small local clusters of activity propagate like traveling waves slowly within Vp (see supplementary materials, movie 2). The propagation of this activity wave has a definite origination point and propagation direction with a speed of approximately 0.01 m/s, which is comparable to the speed measured in cortical slices (Petersen et al. 2003; Sanchez-Vives and McCormick 2000). This is a reflection of the propagation of activity largely through local interlaminar connections. Second, the activity propagated rapidly across the entire cortical area Vp, attributed to the accelerated spread of multiple clusters of activity mediated largely through intralaminar horizontal connections. These connections cause the depolarization of the up-state to propagate throughout Vp with an estimated speed of about 1.6–4.0 m/s. The propagation of the slow oscillation and the observed range of speeds are compatible with experimental data measured in human EEG showing that the slow oscillation is a traveling-wave phenomenon (Massimini et al. 2004). Finally, propagation occurs between cortical areas Vp and Versus (not shown), although it is not possible to estimate the corresponding propagation speed from the model. The precise origination site and propagation path is variable between each cycle and the next.

Intrinsic and synaptic currents underlie the alternation between up- and down-states

The 3 primary active intrinsic currents underlying the up- and down-state in L5–6I_B neurons are I_h , I_{DK} , and $I_{Na(p)}$ (Fig. 5D). These currents fluctuate and reflect the different stages of the slow oscillation, with $I_{Na(p)}$ and I_{DK} making the strongest contribution to the membrane potential. The primary depolarizing intrinsic factor is a voltage-dependent sodium current $I_{Na(p)}$. The half point activation for $I_{Na(p)}$ was set to -55.0 mV, but the conductance begins to increase slightly at voltages as low as -80 mV. Although the current is very small at this voltage, it has an accumulative and amplifying effect as it is integrated into the membrane potential, gradually increasing and pushing the cell to a persistent depolarized state. The primary hyperpolarizing intrinsic factor is the depolarization-activated potassium current I_{DK} . Because this current is activity dependent, the amount of depolarization and spiking influence the strength of I_{DK} , thus determining the degree of hyperpolarization. With an increased firing rate, I_{DK} increases significantly. Similarly, with low levels of depolarization or spiking, the I_{DK} current remains weak. $I_{Na(p)}$ and I_{DK} tend to covary balancing each other during the up-state. The hyperpolarization-activated current I_h becomes active during the down-state and slowly activates, providing a small depolarizing current. Model neurons in other cortical layers lack I_h , although they

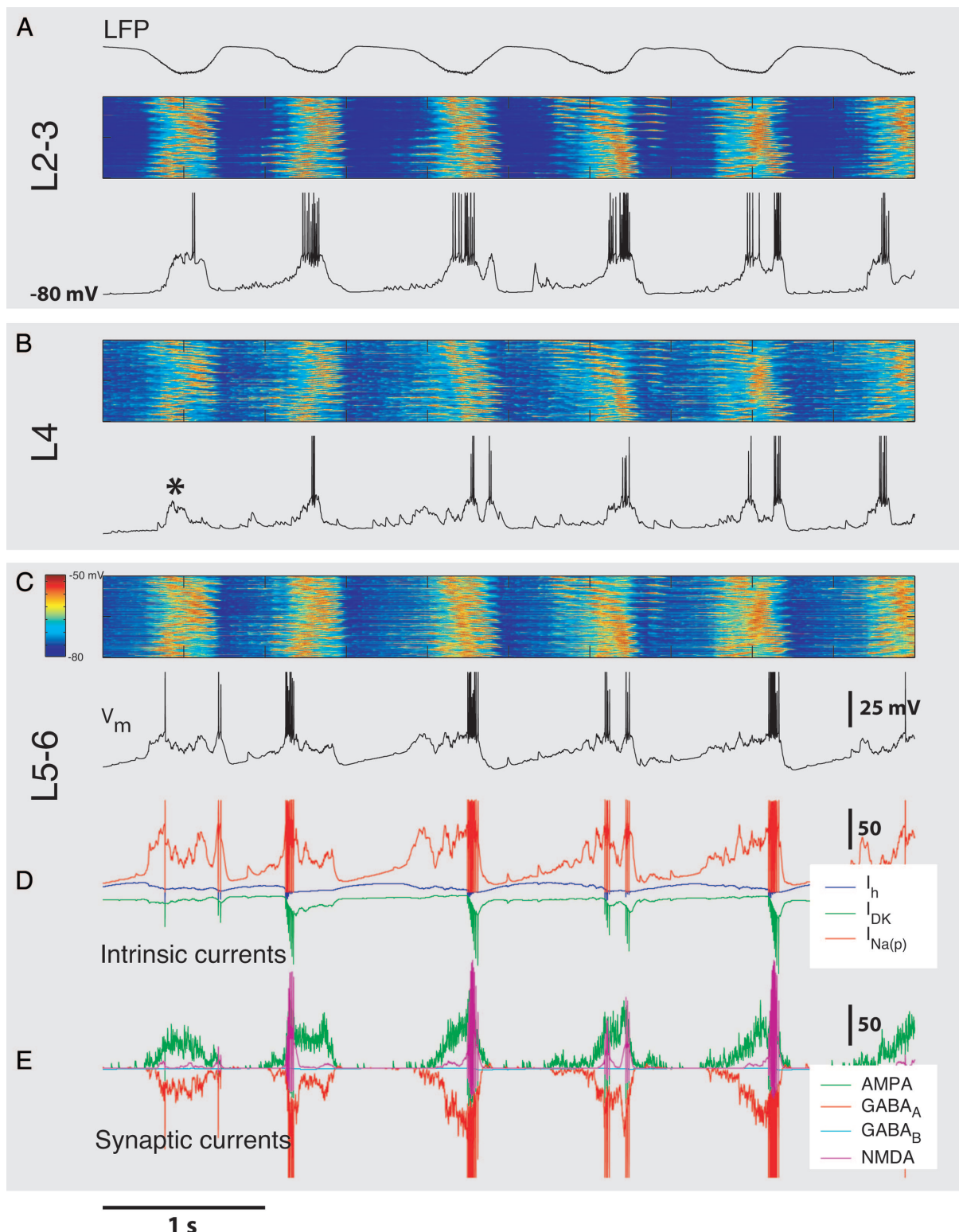


FIG. 5. Regular slow oscillations in the sleep mode. **A–C:** representative activity during the sleep mode shows regular, stable slow oscillations at a frequency of about 0.9–1.1 Hz. Network maintains a stable regimen of alternating up- and down-states throughout the cortical circuitry. LFP (**A, top**) reflects the synchronization of all neurons throughout the cortical model. Membrane potential rasters for 100 neurons selected from each layer (**A: L2–3, B: L4; and C: L5–6**) of the model Vp cortex show that the slow oscillation is a population level phenomenon. Intracellular traces show a variety of up-states in individual neurons including some without any spikes at all (*, as observed in vivo). Small depolarizations seen in some traces (L4 and L5–6) during the down-state reflect synaptic input that continues to arrive from Tp. Individual synaptic (**D**) and intrinsic (**E**) current traces show the component currents of the membrane potential for the selected cell in L5–6. Note the activation of excitatory α -amino-3-hydroxy-5-methyl-4-isoxazolepropionic acid (AMPA) and inhibitory γ -aminobutyric acid-A ($GABA_A$) synaptic currents during the up-state. Note also the activation of $I_{Na(p)}$ and I_{DK} intrinsic currents during the up-state and the very low activation of all currents during the down-state.

contain the remaining intrinsic currents and similar activity profiles.

Figure 5E shows the primary categories of synaptic input: the excitatory currents AMPA, NMDA and the inhibitory currents GABA_A and GABA_B. AMPA and GABA_A dominate during the up-state and they tend to maintain a balance with each other. Note that NMDA occurs independently of these 2 during the up-state and plays a significant depolarizing role during periods of strong activation. GABA_B is rarely active during the up-state, although it can become active during seizure-like activity (see following text). During the down-state, large EPSPs (reflecting synaptic input from the thalamus) and the low-amplitude synaptic minis (representing synaptic quantal release) are visible in L5–6 synaptic current traces (especially AMPA). Throughout the up-state synaptic currents are held in check by synaptic depression, an activity-dependent decrease in synaptic strength that depends on presynaptic firing rates.

The distribution of the membrane potential changes between the waking and sleep modes

Spontaneous activity patterns in individual neurons show dramatically different distributions between the waking mode and the sleep mode. In the waking mode, the membrane potential of model neurons throughout the model cortex fluctuates near firing threshold and the cells spike irregularly (Fig. 6A). The histogram of the membrane potential of a representative neuron shows an even distribution around the mean of -60 mV, consistent with in vivo intracellular recordings in cats (Steriade et al. 2001). During the sleep mode, by contrast, each cell changes activity patterns and alternates between depolarized (-60 mV) and hyperpolarized (-80 mV) phases (Fig. 6B). The membrane potential distribution becomes strikingly bimodal, illustrating the bistable nature of the network during the slow oscillation. The bimodal distribution of the membrane potentials is consistent with data recorded during natural sleep in vivo (Steriade et al. 2001). Because of the long duration of the down-states the peak of the distribution during the hyperpolarized phase is larger than that observed in vivo. This is to be expected because of the small portion of cortex being modeled. In vivo, the frequency of the up-states increases and the duration of down-states decreases with the size of the intact preparation (Timofeev et al. 2000).

Spontaneous firing rates vary throughout the layers of the model and change between the waking and sleep modes

In the waking mode, model neurons exhibit average spontaneous firing rates that vary throughout the layers of the network (Fig. 6C, left). L4, the primary input layer, has the highest firing rate in the cortex (10 ± 8.5 spikes/s). L5–6, which receives slightly less dense projections from the thala-

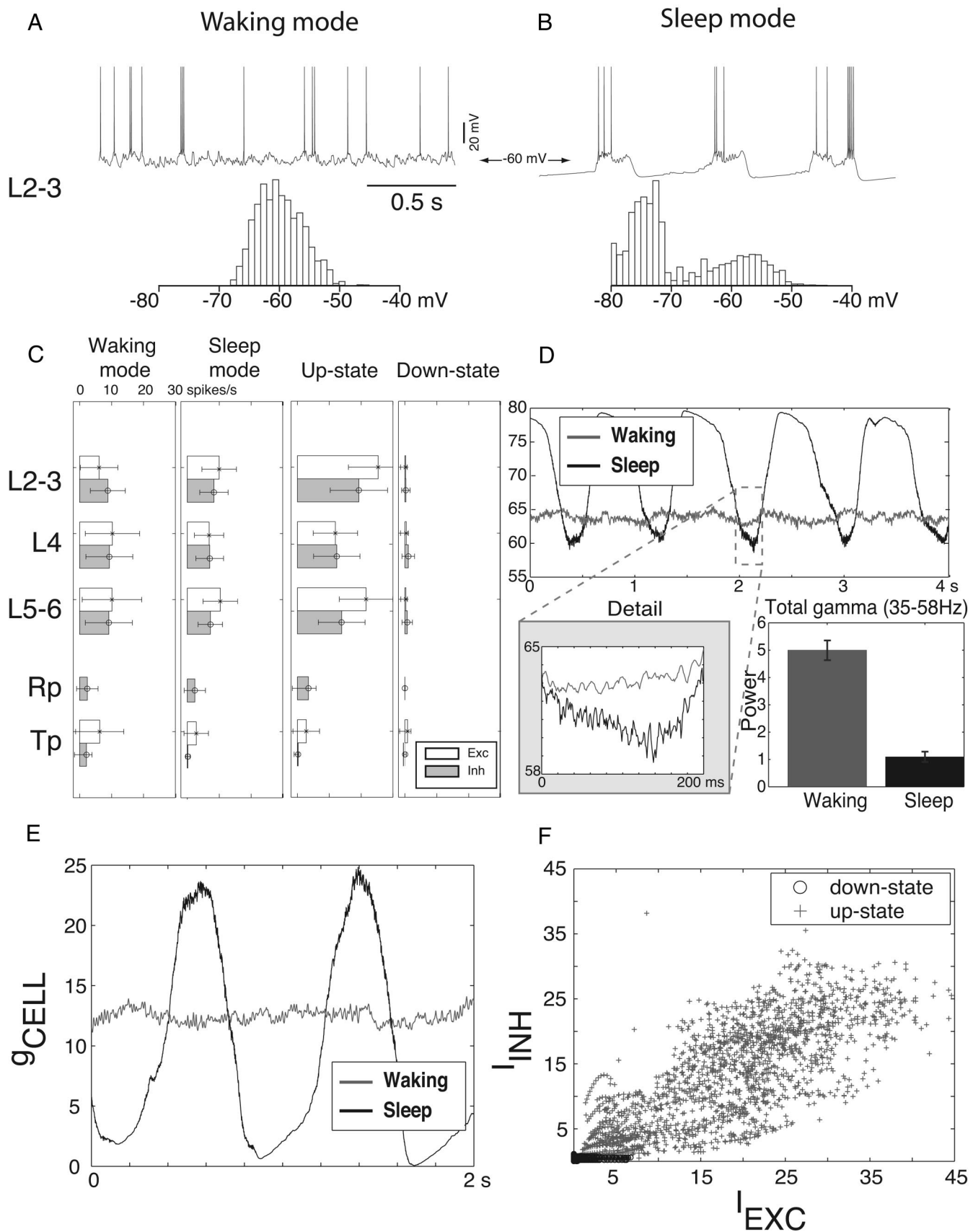
mus, has a lower activity rate (9 ± 9.3 spikes/s). L2–3, the superficial layer, is more quiet, with a mean firing rate of approximately 6 ± 5.8 spikes/s. This distribution of firing rates in the model is consistent with in vivo recordings from V1 of alert monkeys, although the model exhibits slightly higher firing rates in the supragranular layer (6 ± 5.8 vs. 2 – 3 spikes/s) (Snodderly and Gur 1995) (to our knowledge, data are not available for the cat). In the sleep mode (Fig. 6C, right), the mean rate and laminar distribution of neural firing change slightly. Neurons in L2–3 increase their firing rate, whereas the firing rate for L4 excitatory neurons decreases. A slight increase is also seen in the firing rate for excitatory neurons in L5–6. Figure 6C shows the distribution of firing rates during the up- and down-state of the sleep mode. L2–3 shows the highest firing rate (25 ± 10.1 spikes/s). L4 is the least active cortical population firing at 11 ± 8.2 spikes/s. L5–6 fires at elevated rates comparable to L2–3 (22 ± 9.3 spikes/s). Overall, firing rates are elevated above the level seen during waking (10–25 Hz) during the up-state, whereas the network is strikingly inactive and firing rates are essentially zero during the down-state. This is consistent with experimental observations of the firing rate during the slow oscillation in vivo (Steriade et al. 1993). The most active populations during the up-state are L2–3 and L5–6, reflecting the dominance of corticocortical input during the sleep mode, in contrast to the dominance of thalamocortical input during the waking mode.

Activated states give rise to gamma frequency activity in the waking and sleep modes

Figure 6D shows that high-frequency fluctuations occur during both the waking and sleep modes. In the waking mode, bursts of activity are seen both when a stimulus is applied and during spontaneous ongoing activity. This activity consists of synchronized fluctuations in membrane potential and spike discharges across entire neural populations. In the sleep mode, high-frequency fluctuations in the LFP are present during the up-state of the slow oscillation. This is consistent with the description of the generation of gamma frequency activity during activated states in both wakefulness and sleep in vivo (Steriade 2000). Figure 6D (bar plot) compares the total power in the γ range of 35–58 Hz (during 4-s epochs) in the waking and sleep modes. Consistent with recent studies in humans (Cantero et al. 2004), there is much less gamma activity during the up-states of the slow oscillation of the sleep mode than there is in the waking mode ($n = 10$ epochs; $P < 0.0001$, *t*-test).

Gamma frequency oscillations are generated in the model during depolarized states. As indicated by further simulations, a key parameter governing the generation of gamma is the kinetics of GABA_A receptors. Strong depolarization and activation of excitatory neurons causes a strong activation of

FIG. 6. Cellular membrane potentials, firing rates, local field potential, and excitatory and inhibitory currents during the waking mode and the sleep mode. A and B: membrane potential traces (*top*) and histogram (1-kHz sampling rate, 1 mV/bin) of V_m (*bottom*) for an individual cell in the waking mode (A) and in the sleep mode (B). Note the bimodal distribution of V_m in the sleep mode. C: average firing rates for 1,600 excitatory and inhibitory cells in each layer of the network in the waking mode and the sleep mode (*left*). Firing rates computed during up- and down-states of the sleep mode (*right*). D: high-frequency activity in the LFP occurs during both the waking mode and the up-state of the sleep mode. Much less gamma (35–58 Hz) is present during sleep (during the up-states) as compared with waking ($n = 10$ epochs of 4 s; $P < 0.0001$, *t*-test). E: conductances for excitatory cells are moderate during the waking mode, low during the down-state, and high during the up-state (average cellular conductances for $n = 1,600$ cells in layer L2–3). F: balance of excitatory and inhibitory synaptic currents during the slow oscillation. Excitatory and inhibitory currents for a single L5–6 cell (1-ms samples for a 1-s epoch) are plotted vs. each other during the sleep mode. Note that the currents are balanced during both the up- and down-states of the sleep mode.



GABA_A channels that serve to pace excitatory firing in a synchronized oscillation. Specifically, the rise time of the GABA_A postsynaptic potential determines the frequency of gamma-range oscillations during the presentation of a stimulus or during the depolarized phase of the sleep mode (data not shown). The role of GABA_A in the model during waking is consistent with both physiological and theoretical studies (Traub et al. 2003; Whittington et al. 2000). The network interactions governing the emergence of this rhythm have been explored in an earlier paper (Lumer et al. 1997b).

Cellular conductances change with activity mode and excitatory and inhibitory synaptic currents are balanced in both the waking and sleep modes

During the waking mode, the average cellular conductance for excitatory cells ($n = 1,600$; L2–3 cells, summed intrinsic and synaptic conductances) is steady at a moderate level, whereas in the sleep mode the conductances alternate between high and low levels reflecting the up- and down-states of the slow oscillation (Fig. 6E). The conductances during the up-state of the sleep mode are nearly twice that of waking, whereas the conductances at the beginning of the down-state are extremely low. These values are consistent with measurements made *in vivo* showing that the input resistance (conductance $^{-1}$) during the up-state is significantly lower than that of wakefulness (Contreras et al. 1996; Steriade 2003; Steriade et al. 2001). Figure 6F shows the excitatory and inhibitory synaptic currents on a model pyramidal cell during both an up- and down-state. Excitatory and inhibitory currents balance each other throughout the slow oscillation. This is consistent with previous theoretical studies concerning the role of excitation and inhibition during activated states (van Vreeswijk and Sompolinsky 1996).

Firing intervals during activated states are highly irregular

We computed the coefficient of variation (CV) of the inter-spike interval (ISI) for spike trains recorded throughout the model cortex during both the waking mode and the up-state of the sleep mode (not shown). The variability was high ($CV \geq 1$) for most model neurons during wakefulness with a mean of $CV = 1.26$; $n = 4,800$. During the up-state, the variability was similarly high ($CV = 1.41$; $n = 4,800$). The slight increase in the CV during sleep may be a reflection of the increased “burstiness” of IB cells in L5–6 attributed to the hyperpolarized state. This variability during both the waking mode and the up-state is consistent with experimental observations. Recent work *in vitro* has shown that the ISI of regular spiking neurons during up-states is highly variable ($CV = 1.74$; $n = 6$) (Shu et al. 2003). Neurons recorded *in vivo* from the primary visual and extrastriate cortices of the awake behaving macaque monkey also exhibit highly variable ISIs (Softky and Koch 1993). Indeed, variable firing patterns occur *in vivo* under numerous conditions and appear to be

characteristic of high-conductance states (Destexhe et al. 2003; Shadlen and Newsome 1998).

Persistent sodium currents ($I_{Na(p)}$), hyperpolarization-activated cation currents (I_h), and synaptic activity in cortical cells initiate the up-state

To identify the key players involved in the initiation, maintenance, and termination of the slow oscillation, we performed a number of parameter manipulations on the network in the sleep mode. We used as a control condition a 1.5-s window of the slow oscillation starting from exactly the same initial conditions for each manipulation, including the same random number generator seed. In the absence of any manipulation, the network exactly reproduces the control condition every time it is simulated starting from these initial conditions. Therefore until the point at which a parameter is manipulated, the activity at all levels in the network is identical. This allows us to examine the effect of the key parameters on network activity in a precise and reproducible manner.

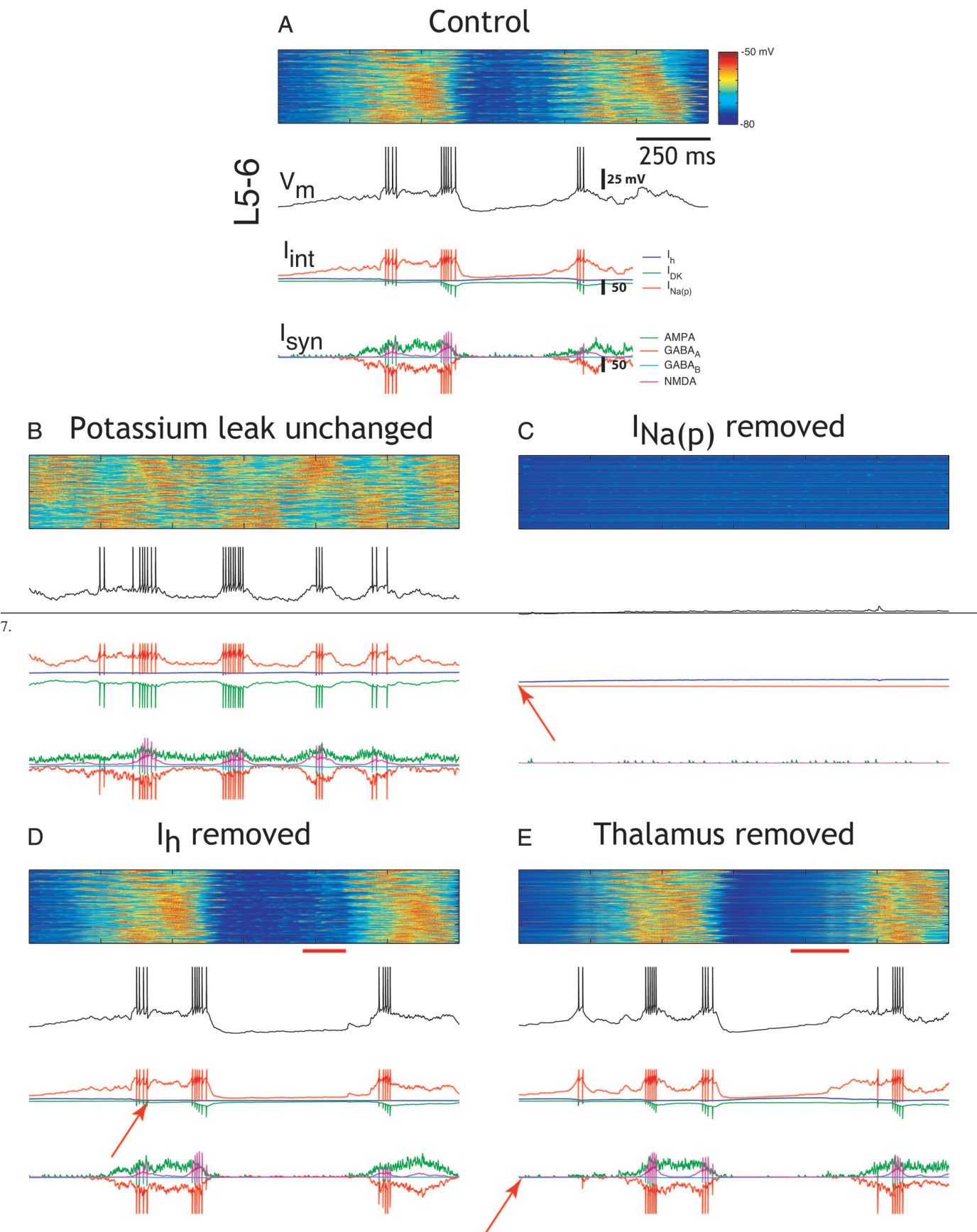
As shown in Fig. 7A, $I_{Na(p)}$, I_h , synaptic minis, and thalamocortical EPSPs all provide depolarizing input to cortical neurons (L5–6 and L4), causing them to start firing and leading to a cascade of synaptic activity which initiates the slow oscillation throughout the network.

Figure 7B shows the important role of the potassium leak current in the transition from the waking mode to the sleep mode. The model starts from the same initial conditions as the control condition, but with the potassium conductance set to waking levels ($g_{KL} = 1.0$). The activity produced in this condition strongly resembles the up-state but without any down-state interrupting the periods of depolarization. The bistability between up- and down-states in the network is lost.

Blocking $I_{Na(p)}$ prevents any activity from developing (Fig. 7C). Synaptic minis and thalamocortical EPSPs are unable to cause a cell to become sufficiently depolarized and fire. Lack of $I_{Na(p)}$, neurons are incapable of reaching firing threshold and initiating the up-state and they remain hyperpolarized at about -80 mV. This is consistent with the finding that spontaneous up-states in cortical slice preparations are completely abolished when $I_{Na(p)}$ is blocked (Mao et al. 2001).

Under control conditions, the cells in L5–6 endowed with I_h are more depolarized and therefore tend to be the first to fire. When I_h is blocked, the onset of the slow oscillation is delayed by over 100 ms (Fig. 7D). This increased duration of the down-state persists after several cycles, thus reducing the frequency of the slow oscillation (not shown). This slowing effect is consistent with experimental studies showing that the frequency of up-states is reduced when I_h blockers are applied (Mao et al. 2001). The model behavior is also consistent with the observation that infragranular layers tend to be more depolarized and in slice preparations, the slow oscillation originates from cells in these layers (Sanchez-Vives and McCormick 2000).

FIG. 7. Intrinsic and synaptic mechanisms involved in the initiation of the up-state. A: control condition. Top to bottom: membrane potential rasters for 100 neurons in L5–6; intracellular trace for a single neuron in L5–6; intrinsic currents underlying the intracellular trace; synaptic currents underlying the intracellular trace. B: result of transitioning to the sleep mode without modifying the potassium leak conductance. Notice the persistent up-state-like activity. C: persistent sodium $I_{Na(p)}$ is removed for the entire simulation. Note that no cell fires when this current is blocked. D: I_h current was removed at the time indicated by the red arrow. Note the slowing of the arrival of the up-state (by 100 ms compared with the control condition; see red line below raster). E: thalamic input is removed for the entire simulation. Note the slowing of the slow oscillation (by nearly 250 ms compared with the control condition; see red line below raster) resulting from the removal of this depolarizing input.



The removal of the thalamus, which provides excitatory input to both L5–6 and L4, causes a slight hyperpolarization in L5–6 (Fig. 7E) and L4 (not shown) membrane potentials, slowing the initiation of the slow oscillation by about 250 ms. Nonetheless, the slow oscillation still emerges and intrinsic and synaptic activity resembles the control condition (Fig. 7A). This demonstrates that the initiation of the slow oscillation in the model is purely cortical, consistent with experimental observations (Mao et al. 2001; Sanchez-Vives and McCormick 2000; Timofeev et al. 2000).

In summary, according to the present simulations, the key to initiating an up-state is the activation of $I_{Na(p)}$ consistent with experimental observations (Timofeev et al. 2000). This can be accomplished using a variety of means, including spontaneous quantal release “minis,” synaptic input from other cortical and thalamic areas, or intrinsic hyperpolarization-activated I_h currents. The experimental evidence for the mechanisms responsible for the initiation of the up-state points to both intrinsic and synaptic mechanisms. Compte et al. (2003) suggested that neurons within the cortex are spontaneously active and the coincident activation of a sufficient number of neurons triggers the up-state. The spontaneous activity in infragranular cells is attributed to intrinsic conductances present in these cells (Mao et al. 2001; Sanchez-Vives and McCormick 2000). Infragranular IB cortical cells contain intrinsic conductances, such as I_h , $I_{Na(p)}$, and I_{KCa} , which are responsible for intrinsic bursting properties (Franceschetti et al. 1995; Silva et al. 1991). Of these, $I_{Na(p)}$ appears to be the most important in generating intrinsic bursts (Franceschetti et al. 1995). Moreover, blocking I_h and $I_{Na(p)}$ abolishes spontaneous activity in cortical slice preparations (Mao et al. 2001).

Both intrinsic and synaptic currents maintain the up-state

During the up-state, a number of currents—synaptic and intrinsic—are active (Fig. 8A). Note that AMPA, NMDA, and $GABA_A$ are all active during the up-state. Also note the activation of intrinsic depolarizing [$I_{Na(p)}$] and hyperpolarizing (I_{DK}) currents.

Blocking all intracortical AMPA currents causes a failure in the up-state (Fig. 8B) and terminates the slow oscillation, although there continues to be spontaneous activity in L5–6 arising from intrinsic currents. This is consistent with experimental evidence showing a termination of the slow oscillation when non-NMDA glutamatergic channels are blocked, yet spontaneous activity persists in infragranular cells (Sanchez-Vives and McCormick 2000).

In Fig. 8C, blocking NMDA leads to a disruption of the up-state. The depolarizing influence of NMDA plays an important role in determining the duration of the up-state. A mixture of AMPA and $I_{Na(p)}$ causes sporadic depolarizations but network activity is strikingly desynchronized and fails to exhibit a network-wide synchronized up-state. This is consistent with experimental data showing that blocking NMDA can interfere with the generation of the slow oscillation and causes

greatly shortened up-states in individual cells (Steriade et al. 1993).

When $GABA_A$ is blocked during the up-state (Fig. 8D), a high burst of activity is produced, followed by a rapid, synchronous termination of the depolarized phase. With the removal of this inhibition, AMPA and NMDA dominate, inducing a high-frequency burst until the inhibitory I_{DK} current overwhelms it. This suggests that $GABA_A$ plays a crucial role in maintaining the balance of excitation and inhibition during the up-state. During this intense burst of activity, $GABA_B$ receptors also become highly activated (Fig. 8D, synaptic currents). $GABA_B$ is usually minimally active during the up-state and the waking mode, but during this seizurelike activity, it plays a significant role in limiting the runaway excitation.

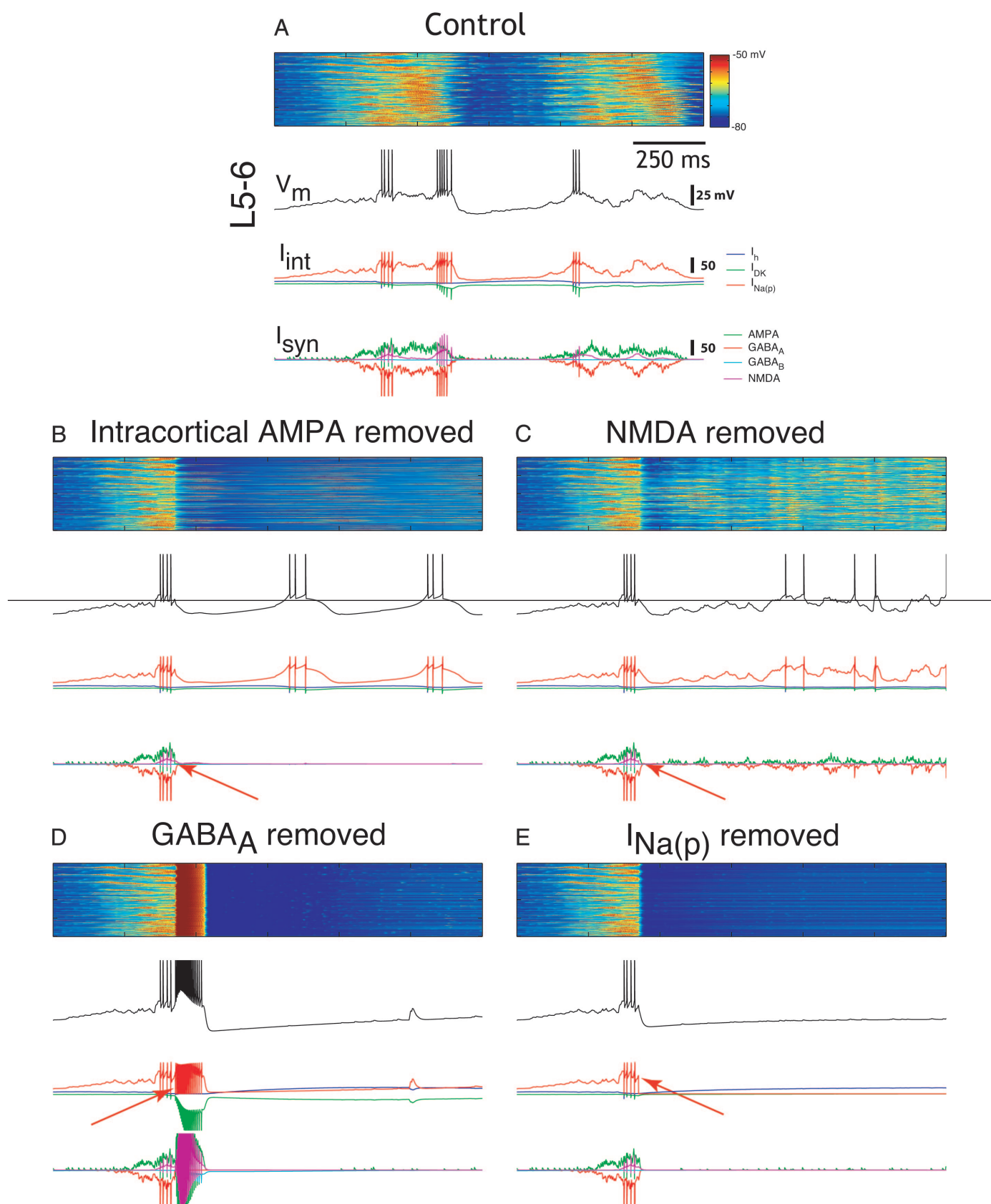
Blocking $I_{Na(p)}$ (Fig. 8E) during an up-state immediately terminates the depolarized phase. The network rapidly becomes hyperpolarized, suggesting that $I_{Na(p)}$ is critical not only for initiating the up-state (as described above) but also for its maintenance.

Depolarization-activated potassium currents (I_{DK}) and synaptic depression terminate the up-state

Intrinsic and synaptic factors are both involved in the termination of the up-state. The primary factor is the hyperpolarizing depolarization-activated potassium current I_{DK} , which is activated during the up-state (Fig. 9A). Because the strongest influx of calcium and sodium occurs during a spike, I_{DK} increases most rapidly during periods of firing. This means that periods of rapid firing substantially contribute to the termination of the up-state at the level of an individual cell. Figure 9B shows the result of blocking I_{DK} in the midst of an up-state. The duration of the up-state is lengthened by several hundred milliseconds and the down-state is shorter compared with the control condition. The model activity also becomes desynchronized with the removal of I_{DK} . The frequency of the oscillation increases to 2–4 Hz. This increase in the oscillation frequency is consistent with that observed *in vitro* after the application of β -adrenergic agents, which block slow AHPs in cortical neurons and replace the slow oscillation with a faster 2- to 3-Hz rhythm (Brumberg et al. 2000).

Synaptic depression, which reduces the amount of synaptic current based on recent presynaptic activity (see METHODS), also plays an important role in the termination of the up-state as well as in the synchronization of the slow oscillation. Blocking synaptic depression altogether causes some neurons to fail to terminate the up-state and the network becomes more noisy and desynchronized (Fig. 9C). In Fig. 9D, the rate of synaptic depression is increased to 4-fold its normal level (used for control and waking conditions). The amplitude of synaptic currents is reduced and continues to decrease during the up-state. As a result, the up-state becomes significantly shorter (about 1/3 less) than during the control oscillation (Fig. 9A). The time to recover from synaptic depression also influences

FIG. 8. Intrinsic and synaptic mechanisms involved in the maintenance of the up-state. *A*: control condition. Notice the persistent activation of $I_{Na(p)}$ and the increased levels of AMPA, N-methyl-D-aspartate (NMDA), and $GABA_A$ during the up-state. *B*: removing AMPA immediately terminates the up-state. Note that intrinsic bursting remains in L5–6 cells arising from $I_{Na(p)}$ and I_{DK} . *C*: removing NMDA terminates the up-state. Note that the individual cells continue to produce up- and down-states that are shorter and the network becomes desynchronized. *D*: removing $GABA_A$ causes high-intensity seizurelike bursts. Although subsequent seizures are not visible because of the timescale, they do repeat at long intervals (about 1 s). *E*: removing $I_{Na(p)}$ immediately silences the entire cortical network. Red arrows indicate the time of the manipulation.



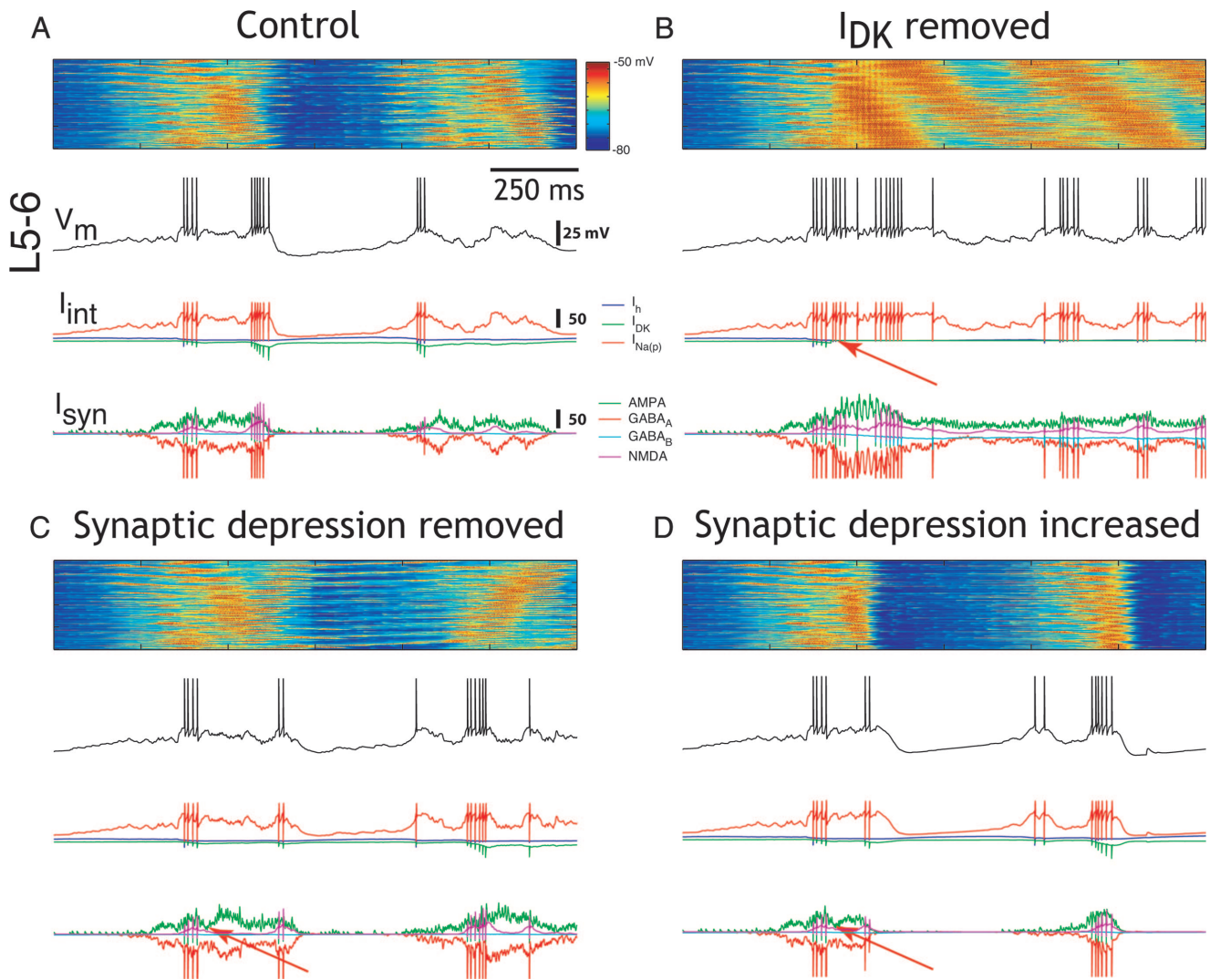


FIG. 9. Intrinsic and synaptic mechanisms involved in the termination of the up-state. *A*: control condition. Note the gradual decrease in synaptic currents and the increase of I_{DK} during the course of the up-state. *B*: I_{DK} is turned off during the up-state. Note the replacement of the slow oscillation with a higher-frequency rhythm (2–4 Hz). *C*: synaptic depression is turned off completely. Note the desynchronized termination of the up-state and the subsequent desynchronization of the slow oscillation. *D*: rate of synaptic depression is increased 4-fold at the beginning of the simulation. Note the shortened duration of the up-state. Red arrows indicate the time of the manipulation.

the initiation of a new up-state as seen by the extended time spent in a down-state despite the strong activation of $I_{Na(p)}$.

The mechanisms that determine the termination of the up-state are not clear from experimental data. Computational studies have suggested that both potassium currents (Compte et al. 2003) and synaptic depression (Bazhenov et al. 2002) are important. Our model predicts that they each play an important role. In the model, activity-dependent potassium currents are essential not only for terminating the up-state, but also for maintaining the balance of excitation and inhibition for its duration. In addition, synaptic depression appears to be important in the termination of the up-state as well as in the overall synchronization of the slow oscillation.

Corticocortical connections influence the synchronization and amplitude of the slow oscillation

In the control condition, the network is highly synchronized and produces clearly defined slow oscillations (Fig. 10A). The

LFP reflects this synchronization and the alternation of activated and inactivated states is apparent in the intracellular recording of a cell in L2–3. The slow oscillation is apparent in all 3 layers of cortex. The autocorrelation shows the strong periodicity of the slow oscillation at a frequency of about 1 Hz. To test the dependency of this synchronized activity on corticocortical connections, we blocked 2 sets of connections. The first is the set of horizontal intraareal excitatory connections, which link neighboring neurons within the same cortical area. The second is the set of long-range excitatory connections connecting the 2 cortical areas (Vp and Vs).

Intraareal connections

Blocking all horizontal excitatory connections within the primary cortical area Vp causes the network to rapidly desynchronize, although individual cells continue to produce both up- and down-states (Fig. 10B). These connections are blocked by setting the conductance for all AMPA and NMDA channels

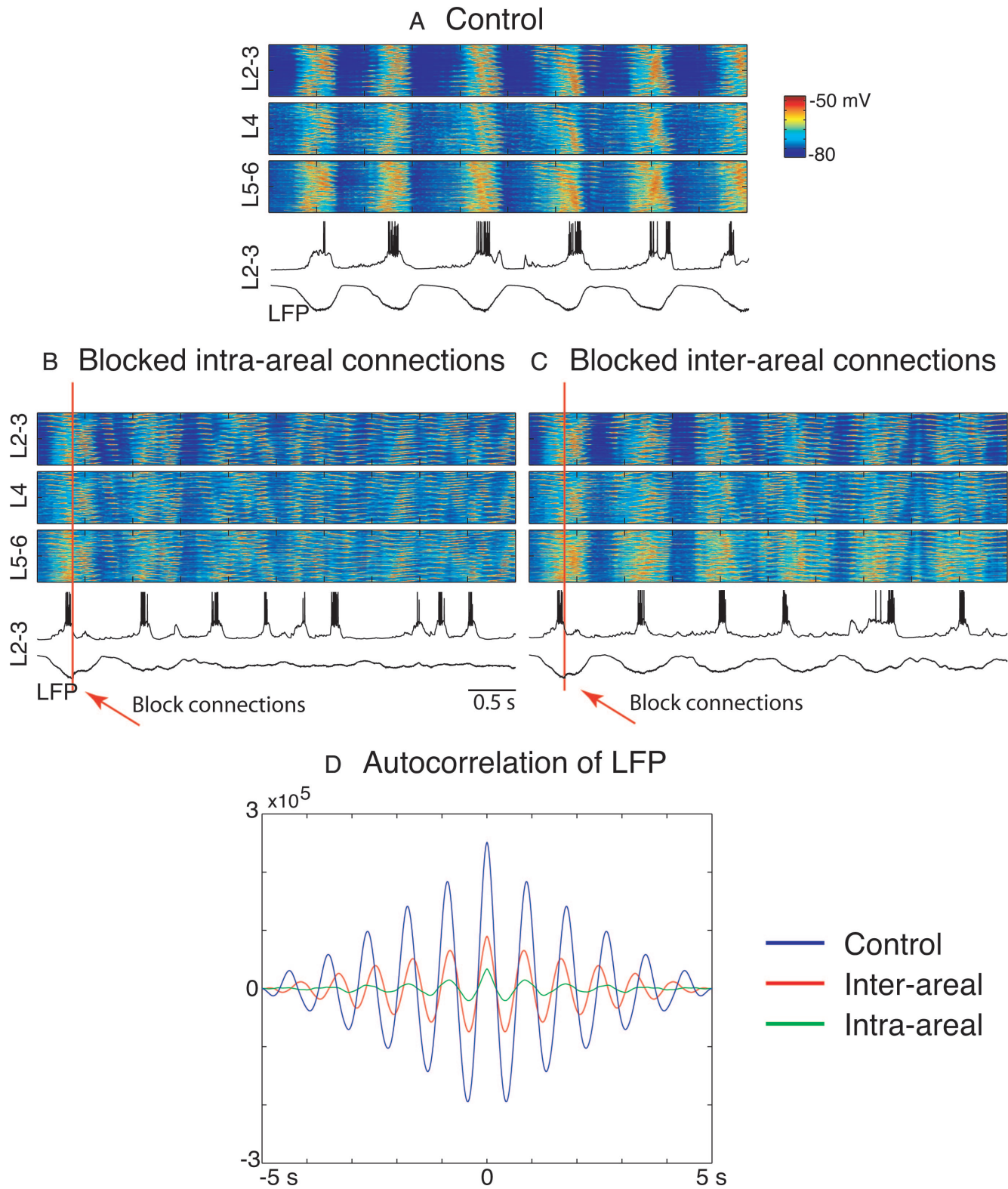


FIG. 10. Synchronization of the slow oscillation through corticocortical connections. *A*: membrane potential rasters for 100 neurons from each layer L2–3, L4, and L5–6. LFP for L2–3 and a representative intracellular trace (V_m) from L2–3 for a duration of 5 s. *Top* shows the control condition. Note that the regular stable oscillation reflected at all levels of the network. *B*: after blockade of horizontal intralaminar connections. Note that the network becomes desynchronized, but individual neurons continue to produce up- and down-states, albeit of shorter duration and reduced amplitude. *C*: after blockade of interareal corticocortical connections. Note that the network gradually becomes desynchronized, although individual cells continue to produce the up- and down-states. Notice the increased synaptic activity during the down-state. *D*: autocorrelation of LFP (from *A*, *B*, *C*) for both control and blocked conditions (10 s). Note that the control condition (blue) is highly synchronized. After blocking intraareal connections (green) synchronization falls off dramatically, whereas blocking interareal connections produces an intermediate level of desynchronization.

associated with horizontal connections within Vp or Versus to zero. All vertical and interareal connections remain intact. Notice the decrease in amplitude of the LFP as the network becomes progressively desynchronized. Intracellular traces show how the up-states of the slow oscillation are shortened as a result of the lack of synchronizing input from neighboring cells. The autocorrelation of the LFP shows that cutting intraareal connections dramatically reduces the normal strong synchronization (Fig. 10D). In addition, the average hyperpolarization during the down-state (computed by averaging the membrane potential across all down-states selected from 10 s of sleep mode) is decreased by 63% of the control condition for all cortical neurons. The role of intraareal connections in maintaining and synchronizing the slow oscillation in the model is consistent with experimental data recorded *in vitro* and *in vivo*. Experiments *in vitro* show that activity is propagated and synchronized by horizontal cortical connections (Sanchez-Vives and McCormick 2000). Furthermore, the frequency and regularity of depolarizing events in cortical slabs has been linked to the size of their intact network, suggesting that the frequency of the slow oscillation depends on the extent of the corticocortical network (Timofeev et al. 2000).

Interareal connections

Blocking all interareal connections between Vp and Vs also results in desynchronization, although less marked than that after blocking intraareal connections (Fig. 10C). Blocking these connections consists of setting the conductance of all AMPA and NMDA channels for the connections between Vp and Vs to zero. All intraareal connections remain intact. The LFP continues to display a distinct rhythmicity but its amplitude is greatly reduced. Intracellularly, cells continue to produce the slow oscillation, although the up-state is shortened and down-states become noisier as they reflect the activity of other neurons in the network. Membrane potential rasters show how Vp remains rhythmic but is not entrained in a tight slow oscillation. The autocorrelation of the LFP illustrates the intermediate level of desynchronization arising from blocking interareal connections (Fig. 10D). This intermediate desynchronization is also reflected in a 46% decrease in the average hyperpolarization during the down-state. The results of these manipulations are consistent with experimental data showing that application of lidocaine to corticocortical connections can cause cortical oscillations to become less synchronized (Amzica and Steriade 1995a).

DISCUSSION

We have constructed a large-scale model of the visual thalamocortical system that captures its physiological properties and anatomical organization at multiple levels: from the level of intrinsic cellular currents and synaptic conductances to that of the connectivity within and between cortical and thalamic areas. Our goal was to provide a coherent account, within a single model, of the functioning of the thalamocortical system in waking and sleep.

In the waking mode, the model reproduces experimental observations from waking animals, including the spontaneous irregular firing underlying EEG low-voltage fast activity, the emergence of correlated subthreshold activity reflecting the

functional organization of intracortical connections, the selective response of different neuronal populations to visual stimuli, and the gamma frequency synchronization in evoked responses. The results during waking are consistent with experimental work using intracellular (Azouz and Gray 1999; Jagadeesh et al. 1992), extracellular (Alonso and Martinez 1998; Softky and Koch 1993), optical imaging (Arieli et al. 1995; Kenet et al. 2003; Tsodyks et al. 1999), and EEG techniques (Gray and Singer 1989). The distribution of spontaneous firing rates across different cortical layers is also consistent with experimental data (Snodderly and Gur 1995).

The present work builds on our previous model of orientation selectivity (Lumer et al. 1997b). Briefly, orientation selectivity in this model results from a conventional Hubel and Wiesel arrangement of afferents from oriented patches in the thalamus converging on individual cells in the model cortex such that they define horizontal and vertical receptive fields. Several other computational models have explored the genesis of orientation and directional selectivity (Douglas et al. 1995; McLaughlin et al. 2000; Miller 1994; Somers et al. 1995; Wimbauer et al. 1997a,b; Worgotter and Koch 1991). Although the specific mechanisms yielding orientation selectivity are not the focus of the present paper, it should be emphasized that this model is unique, in that selective responses occur in the context of a 3-layer cortex, reticular nucleus, and thalamus connected by thalamocortical, corticothalamic, and corticocortical projections.

By changing a few parameters that simulate the effects of the reduced release of neuromodulators on certain potassium currents, we show that the same model can transition smoothly between a waking and a sleep mode of firing. In the sleep mode, the model gives rise to slow oscillations at <1 Hz that closely resemble those observed experimentally *in vivo* and *in vitro*, including the bimodal distribution of membrane potentials (Steriade et al. 2001), the irregularity of firing (Shu et al. 2003), the wavelike propagation of the slow oscillation (Massimini et al. 2004; Sanchez-Vives and McCormick 2000), the marked changes in total membrane conductance between the up- and down-states (Contreras et al. 1996), and the preserved balance of excitatory and inhibitory currents throughout the slow oscillation (Sanchez-Vives and McCormick 2000; Shu et al. 2003).

In addition, the model offers a self-consistent, multilevel account of how the slow oscillation is initiated, maintained, and terminated. Specifically, the model suggests that $I_{Na(P)}$ is the single most important current in the initiation and maintenance of the slow oscillation. This is consistent with experimental observations that $I_{Na(P)}$ underlies a broad range of intrinsic activity in cortical neurons (Mao et al. 2001; Stafstrom et al. 1984). There are many mechanisms that can depolarize a neuron sufficiently to activate $I_{Na(P)}$. Intrinsic depolarizing currents such as I_h or synaptic input from the thalamus are 2 possible mechanisms for activating $I_{Na(P)}$. Not all cells in the model are the same and I_h helps the cells in L5–6 initiate the slow oscillation. In an intact system, the synaptic input that could trigger abrupt transitions to an up-state will be much greater because of the strong corticocortical inputs.

Experimental and computational studies have provided differing views of how depolarization-dependent potassium currents and synaptic depression are involved in the termination of

the slow oscillation (Bazhenov et al. 2002; Compte et al. 2003; Sanchez-Vives and McCormick 2000; Timofeev et al. 2000). According to the model, I_{DK} and synaptic depression are jointly important for synchronizing network activity and terminating the up-state. The duration of the down-state is not determined by a simple parameter such as the conductance or time constant of I_{DK} . The up-state requires a balance of excitation and inhibition in the network that must include the hyperpolarizing influence of I_{DK} . In fact, when I_{DK} was blocked, the up-state was altered and the network began to exhibit high-frequency waves of activity. The duration of the down-state depends on the network's ability to initiate a new up-state, which itself is dependent on sufficient synaptic or intrinsic depolarization to overcome the hyperpolarizing potassium currents (I_{KL} and I_{DK}) and activate the depolarizing sodium current $I_{Na(p)}$. The intricate balance of excitatory and inhibitory synaptic and intrinsic mechanisms determines the time course of the down-state.

The simulations also show that the synchronization and amplitude of the slow oscillation are dependent on the strength of both intra- and interareal corticocortical connections, confirming and extending experimental results both *in vitro* (Sanchez-Vives and McCormick 2000) and *in vivo* (Amzica and Steriade 1995a). Moreover, cortical connectivity in the model plays an important role in determining the spontaneous activity patterns during both the waking and the sleep mode. In the waking mode, spontaneous activity is injected from peripheral inputs and filtered through thalamocortical connectivity. This results in patterns of spontaneous subthreshold depolarizations and correlated firing that reflect the organization of orientation selectivity. In the sleep mode, spontaneous activity during the up-state of the slow oscillation is much less selective because it is generated intrinsically within the entire cortex and the thalamus is profoundly hyperpolarized.

The model also indicates that the specific balance of excitation and inhibition that is active during waking is essential for producing balanced up-states during sleep. When the balance of excitation and inhibition in the waking mode is disrupted, the sleep mode is similarly disrupted and the network tends to seizurelike activity. The network is particularly prone to any instability during sleep because of the bistable nature of this mode.

Finally, in the model NMDA plays a critical role in maintaining the up-state and synchronizing the slow oscillation. This observation may seem to be inconsistent with the fact that most available data concerning the slow oscillation have been recorded under conditions of ketamine–xylazine anesthesia (Steriade et al. 1993), where ketamine is known to be an NMDA antagonist. Xylazine, however, is an agonist of the $\alpha 2$ subunit of GABA_A receptors. In the model, when NMDA blockade was associated with an increase in GABA_A conductances (with an additional small augmentation of AMPA conductances), slow oscillations could be observed, albeit with reduced up-state durations and with a tendency to produce seizurelike activity.

Other computational models have examined the mechanisms responsible for the generation of the slow oscillation. Bazhenov et al. (1998, 1999, 2000, 2002) studied sleep rhythms in a simulated one-dimensional thalamocortical system during both activated and inactivated states. Compte et al. (2003) modeled a one-dimensional strip of cortical neurons, lacking a thalamic architecture, which undergoes a slow oscillation. Besides being

larger (65,000 neurons vs. a few hundreds), the present model is 3-dimensional, with a topographically organized cortex subdivided into 3 layers. This has allowed us to model the effects of both intra- and interlayer connections. The model also has a higher-order cortical area, Vs, which has allowed us to investigate the effects of corticocortical connections with different layers of origin and termination on the synchronization of the slow oscillation. Because the model cortex is subdivided into functionally specialized minicolumns, we were also able to evaluate the model's performance with oriented stimuli during waking. In this way, we could ensure that the same model producing the slow oscillation in the sleep mode can also produce orientation-selective responses in the waking mode. Despite these differences, at least with respect to the specific mechanisms responsible for the generation of the slow oscillation, the present results and those of previous models are in substantial agreement.

Despite its success in reproducing and integrating experimental and computational results at several different levels, our model, like any other model, has several limitations. For example, although it contains many tens of thousands of neurons and several million connections, the model is still a far cry from real cortical networks, whose size plays a crucial role in determining the frequency and other characteristics of the slow oscillation *in vivo* (Timofeev et al. 2000). The model also lacks detailed dendritic/axonal morphologies and intracellular compartments and ignores the possible role of glial cells (Amzica 2002). Furthermore, in a model this size it is obviously not possible to perform an exhaustive exploration of parameter space.

The development of this model has required an extensive exploration of dozens of possible mechanisms and parameters in the effort to synthesize a unified thalamocortical model that could reproduce as wide of a range of experimental results possible within the constraints of anatomical and physiological data. The process of modeling the slow oscillation started with a system that produced stable low-firing rate spontaneous activity and high signal/noise ratio selective responses to visual stimuli in the waking mode. We retuned the system to incorporate the basic currents and mechanisms—including $I_{Na(p)}$, I_{DK} , and synaptic depression—believed to play important roles in the slow oscillation. Because the up-state of the sleep mode activates the same circuitry underlying the spontaneous and evoked activity of the waking mode, this tuning involved iteratively reestablishing a balance of excitation and inhibition in the system to prevent seizurelike activity during sleep and maintain visual response characteristics of waking. Throughout the evolution of the model, the refinement process was constrained by matching physiological data at the level of intracellular traces, cellular input resistance, extracellular recordings, and LFP. This process converged on a single model that could satisfy the constraints of reproducing experimental data of neural activity during both wakefulness and sleep while modifying parameters influenced only by neuromodulatory changes.

Thus although we tested the robustness of the results to modifications of dozens of different parameters related to synaptic interactions, intrinsic properties, spiking characteristics, axonal delays, and synaptic depression—amounting to more than 3 years of uninterrupted CPU time—we cannot rule out an aberrant behavior for some untested parameter combination. Nevertheless, the fact that parameter choices have been

constrained by anatomical and physiological data at multiple levels, together with the model's ability to reproduce a wide range of experimental data, suggest that the present account of the transition from wakefulness to sleep and for the generation of the slow oscillation is sufficiently in line with actual biological mechanisms. Finally, by providing a single framework within which a broad range of neural interactions can be examined at several different levels in both a sleep and a waking mode, the model provides a powerful platform for further investigations into the role of sleep in information transmission and plasticity (Destexhe and Sejnowski 2001; Steriade and Timofeev 2003; Tononi and Cirelli 2003).

ACKNOWLEDGMENTS

We acknowledge the help of C. G. Habeck during the initial stages of this work and M. Massimini, S. K. Esser, and R. Huber for helpful conversations.

GRANTS

The Swartz Foundation supported a portion of this work and the Neuroscience Research Foundation supported this work in its early stages.

REFERENCES

- Abbott LF, Varela JA, Sen K, and Nelson SB.** Synaptic depression and cortical gain control. *Science* 275: 220–224, 1997.
- Achermann P and Borbely AA.** Low-frequency (<1 Hz) oscillations in the human sleep electroencephalogram. *Neuroscience* 81: 213–222, 1997.
- Ahmed B, Anderson JC, Douglas RJ, Martin KA, and Nelson JC.** Polynerval innervation of spiny stellate neurons in cat visual cortex. *J Comp Neurol* 341: 39–49, 1994.
- Alonso JM and Martinez LM.** Functional connectivity between simple cells and complex cells in cat striate cortex. *Nat Neurosci* 1: 395–403, 1998.
- Amzica F.** In vivo electrophysiological evidences for cortical neuron-glia interactions during slow (<1 Hz) and paroxysmal sleep oscillations. *J Physiol (Paris)* 96: 209–219, 2002.
- Amzica F and Steriade M.** Disconnection of intracortical synaptic linkages disrupts synchronization of a slow oscillation. *J Neurosci* 15: 4658–4677, 1995a.
- Amzica F and Steriade M.** Short- and long-range neuronal synchronization of the slow (<1 Hz) cortical oscillation. *J Neurophysiol* 73: 20–38, 1995b.
- Amzica F and Steriade M.** Cellular substrates and laminar profile of sleep K-complex. *Neuroscience* 82: 671–686, 1998.
- Arieli A, Shoham D, Hildesheim R, and Grinvald A.** Coherent spatiotemporal patterns of ongoing activity revealed by real-time optical imaging coupled with single-unit recording in the cat visual cortex. *J Neurophysiol* 73: 2072–2093, 1995.
- Azouz R and Gray CM.** Cellular mechanisms contributing to response variability of cortical neurons in vivo. *J Neurosci* 19: 2209–2223, 1999.
- Baranyi A, Szente MB, and Woody CD.** Electrophysiological characterization of different types of neurons recorded in vivo in the motor cortex of the cat. II. Membrane parameters, action potentials, current-induced voltage responses, and electrotonic structures. *J Neurophysiol* 69: 1865–1879, 1993.
- Bazhenov M, Timofeev I, Steriade M, and Sejnowski TJ.** Cellular and network models for intrathalamic augmenting responses during 10-Hz stimulation [In Process Citation]. *J Neurophysiol* 79: 2730–2748, 1998.
- Bazhenov M, Timofeev I, Steriade M, and Sejnowski TJ.** Self-sustained rhythmic activity in the thalamic reticular nucleus mediated by depolarizing GABA_A receptor potentials. *Nat Neurosci* 2: 168–173, 1999.
- Bazhenov M, Timofeev I, Steriade M, and Sejnowski TJ.** Spiking-bursting activity in the thalamic reticular nucleus initiates sequences of spindle oscillations in thalamic networks. *J Neurophysiol* 84: 1076–1087, 2000.
- Bazhenov M, Timofeev I, Steriade M, and Sejnowski TJ.** Model of thalamocortical slow-wave sleep oscillations and transitions to activated states. *J Neurosci* 22: 8691–8704, 2002.
- Beaulieu C and Colonnier M.** The number of neurons in the different laminae of the binocular and monocular regions of area 17 in the cat, Canada. *J Comp Neurol* 217: 337–344, 1983.
- Beaulieu C and Colonnier M.** A laminar analysis of the number of round-asymmetrical and flat-symmetrical synapses on spines, dendritic trunks, and cell bodies in area 17 of the cat. *J Comp Neurol* 231: 180–189, 1985.
- Beaulieu C, Kisvarday Z, Somogyi P, Cynader M, and Cowey A.** Quantitative distribution of GABA-immunopositive and -immunonegative neurons and synapses in the monkey striate cortex (area 17). *Cereb Cortex* 2: 295–309, 1992.
- Brumberg JC, Nowak LG, and McCormick DA.** Ionic mechanisms underlying repetitive high-frequency burst firing in supragranular cortical neurons. *J Neurosci* 20: 4829–4843, 2000.
- Bullier J and Henry GH.** Neural path taken by afferent streams in striate cortex of the cat. *J Neurophysiol* 42: 1264–1270, 1979.
- Bullier J, McCourt ME, and Henry GH.** Physiological studies on the feedback connection to the striate cortex from cortical areas 18 and 19 of the cat. *Exp Brain Res* 70: 90–98, 1988.
- Callaway EM and Wiser AK.** Contributions of individual layer 2–5 spiny neurons to local circuits in macaque primary visual cortex. *Vis Neurosci* 13: 907–922, 1996.
- Cantero JL, Atienza M, Madsen JR, and Stickgold R.** Gamma EEG dynamics in neocortex and hippocampus during human wakefulness and sleep. *Neuroimage* 22: 1271–1280, 2004.
- Compte A, Sanchez-Vives MV, McCormick DA, and Wang XJ.** Cellular and network mechanisms of slow oscillatory activity (<1 Hz) and wave propagations in a cortical network model. *J Neurophysiol* 89: 2707–2725, 2003.
- Conde F, Lund JS, Jacobowitz DM, Baimbridge KG, and Lewis DA.** Local circuit neurons immunoreactive for calretinin, calbindin D-28k or parvalbumin in monkey prefrontal cortex: distribution and morphology. *J Comp Neurol* 341: 95–116, 1994.
- Connors BW, Gutnick MJ, and Prince DA.** Electrophysiological properties of neocortical neurons in vitro. *J Neurophysiol* 48: 1302–1320, 1982.
- Contreras D, Timofeev I, and Steriade M.** Mechanisms of long-lasting hyperpolarizations underlying slow sleep oscillations in cat corticothalamic networks. *J Physiol* 494: 251–264, 1996.
- Destexhe A, Bal T, McCormick DA, and Sejnowski TJ.** Ionic mechanisms underlying synchronized oscillations and propagating waves in a model of ferret thalamic slices. *J Neurophysiol* 76: 2049–2070, 1996a.
- Destexhe A, Contreras D, Steriade M, Sejnowski TJ, and Huguenard JR.** In vivo, in vitro, and computational analysis of dendritic calcium currents in thalamic reticular neurons. *J Neurosci* 16: 169–185, 1996b.
- Destexhe A, Rudolph M, and Paré D.** The high-conductance state of neocortical neurons in vivo. *Nat Rev Neurosci* 4: 739–751, 2003.
- Destexhe A and Sejnowski TJ.** *Thalamocortical Assemblies: How Ion Channels, Single Neurons, and Large-Scale Networks Organize Sleep Oscillations*. New York: Oxford Univ. Press, 2001.
- Dinse HR and Kruger K.** The timing of processing along the visual pathway in the cat. *Neuroreport* 5: 893–897, 1994.
- Douglas R and Martin K.** Neocortex. In: *The Synaptic Organization of the Brain* (5th ed.), edited by Shepherd G. Oxford, UK: Oxford Univ. Press, 2003.
- Douglas RJ, Koch C, Mahowald M, Martin KA, and Suarez HH.** Recurrent excitation in neocortical circuits. *Science* 269: 981–985, 1995.
- Dubin MW and Cleland BG.** Organization of visual inputs to interneurons of lateral geniculate nucleus of the cat. *J Neurophysiol* 40: 410–427, 1977.
- Felleman DJ and Van Essen DC.** Distributed hierarchical processing in the primate cerebral cortex. *Cereb Cortex* 1: 1–47, 1991.
- Fitzpatrick D.** Cortical imaging: capturing the moment. *Curr Biol* 10: R187–R190, 2000.
- Fleidervish IA, Friedman A, and Gutnick MJ.** Slow inactivation of Na⁺ current and slow cumulative spike adaptation in mouse and guinea-pig neocortical neurones in slices. *J Physiol* 493: 83–97, 1996.
- Fox K, Sato H, and Daw N.** The location and function of NMDA receptors in cat and kitten visual cortex. *J Neurosci* 9: 2443–2454, 1989.
- Franceschetti S, Guatteo E, Panzica F, Sancini G, Wanke E, and Avanzini G.** Ionic mechanisms underlying burst firing in pyramidal neurons: intracellular study in rat sensorimotor cortex. *Brain Res* 696: 127–139, 1995.
- French CR, Sah P, Buckett KJ, and Gage PW.** A voltage-dependent persistent sodium current in mammalian hippocampal neurons. *J Gen Physiol* 95: 1139–1157, 1990.
- Freund TF, Martin KA, Soltesz I, Somogyi P, and Whitteridge D.** Arborisation pattern and postsynaptic targets of physiologically identified thalamocortical afferents in striate cortex of the macaque monkey. *J Comp Neurol* 289: 315–336, 1989.
- Freund TF, Martin KA, and Whitteridge D.** Innervation of cat visual areas 17 and 18 by physiologically identified X- and Y-type thalamic afferents. I. Arborization patterns and quantitative distribution of postsynaptic elements. *J Comp Neurol* 242: 263–274, 1985.

- Fuentelba P, Timofeev I, and Steriade M.** Prolonged hyperpolarizing potentials precede spindle oscillations in the thalamic reticular nucleus. *Proc Natl Acad Sci USA* 101: 9816–9821, 2004.
- Galarreta M and Hestrin S.** Frequency-dependent synaptic depression and the balance of excitation and inhibition in the neocortex. *Nat Neurosci* 1: 587–594, 1998.
- Galarreta M and Hestrin S.** A network of fast-spiking cells in the neocortex connected by electrical synapses. *Nature* 402: 72–75, 1999.
- Gil Z, Connors BW, and Amitai Y.** Differential regulation of neocortical synapses by neuromodulators and activity. *Neuron* 19: 679–686, 1997.
- Gilbert CD.** Circuitry, architecture, and functional dynamics of visual cortex. *Cereb Cortex* 3: 373–386, 1993.
- Golshani P, Liu XB, and Jones EG.** Differences in quantal amplitude reflect GluR4-subunit number at corticothalamic synapses on two populations of thalamic neurons. *Proc Natl Acad Sci USA* 98: 4172–4177, 2001.
- Gray CM and Singer W.** Stimulus-specific neuronal oscillations in orientation columns of cat visual cortex. *Proc Natl Acad Sci USA* 86: 1698–1702, 1989.
- Henry GH, Salin PA, and Bullier J.** Projections from areas 18 and 19 to cat striate cortex: divergence and laminar specificity. *Eur J Neurosci* 3: 186–200, 1991.
- Hirsch JA and Gilbert CD.** Synaptic physiology of horizontal connections in the cat's visual cortex. *J Neurosci* 11: 1800–1809, 1991.
- Huguenard JR and McCormick DA.** Simulation of the currents involved in rhythmic oscillations in thalamic relay neurons. *J Neurophysiol* 68: 1373–1383, 1992.
- Huguenard JR and Prince DA.** A novel T-type current underlies prolonged Ca^{2+} -dependent burst firing in GABAergic neurons of rat thalamic reticular nucleus. *J Neurosci* 12: 3804–3817, 1992.
- Jagadeesh B, Gray CM, and Ferster D.** Visually evoked oscillations of membrane potential in cells of cat visual cortex. *Science* 257: 552–554, 1992.
- Jones EG.** GABAergic neurons and their role in cortical plasticity in primates. *Cereb Cortex* 3: 361–372, 1993.
- Jones EG.** Thalamic organization and function after Cajal. *Prog Brain Res* 136: 333–357, 2002.
- Kang Y, Kaneko T, Ohishi H, Endo K, and Araki T.** Spatiotemporally differential inhibition of pyramidal cells in the cat motor cortex. *J Neurophysiol* 71: 280–293, 1994.
- Kara P and Reid RC.** Efficacy of retinal spikes in driving cortical responses. *J Neurosci* 23: 8547–8557, 2003.
- Kawaguchi Y.** Physiological subgroups of nonpyramidal cells with specific morphological characteristics in layer II/III of rat frontal cortex. *J Neurosci* 15: 2638–2655, 1995.
- Kawaguchi Y and Kubota Y.** GABAergic cell subtypes and their synaptic connections in rat frontal cortex. *Cereb Cortex* 7: 476–486, 1997.
- Kay AR, Sugimori M, and Llinas R.** Kinetic and stochastic properties of a persistent sodium current in mature guinea pig cerebellar Purkinje cells. *J Neurophysiol* 80: 1167–1179, 1998.
- Kenet T, Bibitchkov D, Tsodyks M, Grinvald A, and Arieli A.** Spontaneously emerging cortical representations of visual attributes. *Nature* 425: 954–956, 2003.
- Kim HG and Connors BW.** Apical dendrites of the neocortex: correlation between sodium- and calcium-dependent spiking and pyramidal cell morphology. *J Neurosci* 13: 5301–5311, 1993.
- Kim U and McCormick DA.** The functional influence of burst and tonic firing mode on synaptic interactions in the thalamus. *J Neurosci* 18: 9500–9516, 1998.
- Kim U, Sanchez-Vives MV, and McCormick DA.** Functional dynamics of GABAergic inhibition in the thalamus. *Science* 278: 130–134, 1997.
- Kisvarday ZF and Eysel UT.** Cellular organization of reciprocal patchy networks in layer III of cat visual cortex (area 17). *Neuroscience* 46: 275–286, 1992.
- Kisvarday ZF and Eysel UT.** Functional and structural topography of horizontal inhibitory connections in cat visual cortex. *Eur J Neurosci* 5: 1558–1572, 1993.
- Kisvarday ZF, Kim DS, Eysel UT, and Bonhoeffer T.** Relationship between lateral inhibitory connections and the topography of the orientation map in cat visual cortex. *Eur J Neurosci* 6: 1619–1632, 1994.
- Kisvarday ZF, Toth E, Rausch M, and Eysel UT.** Orientation-specific relationship between populations of excitatory and inhibitory lateral connections in the visual cortex of the cat. *Cereb Cortex* 7: 605–618, 1997.
- Krubitzer LA and Kaas JH.** Cortical integration of parallel pathways in the visual system of primates. *Brain Res* 478: 161–165, 1989.
- Latawiec D, Martin KA, and Meskenaite V.** Termination of the geniculocalcarine projection in the striate cortex of macaque monkey: a quantitative immunoelectron microscopic study. *J Comp Neurol* 419: 306–319, 2000.
- LeVay S and Gilbert CD.** Laminar patterns of geniculocalcarine projection in the cat. *Brain Res* 113: 1–19, 1976.
- Leventhal AG.** Evidence that the different classes of relay cells of the cat's lateral geniculate nucleus terminate in different layers of the striate cortex. *Exp Brain Res* 37: 349–372, 1979.
- Logothetis NK, Pauls J, Augath M, Trinath T, and Oeltermann A.** Neurophysiological investigation of the basis of the fMRI signal. *Nature* 412: 150–157, 2001.
- Lowel S, Freeman B, and Singer W.** Topographic organization of the orientation column system in large flat-mounts of the cat visual cortex: a 2-deoxyglucose study. *J Comp Neurol* 255: 401–415, 1987.
- Lumer ED, Edelman G, and Tononi G.** Neural dynamics in a model of the thalamocortical system. II. The role of neural synchrony tested through perturbation of spike timing. *Cereb Cortex* 7: 228–236, 1997a.
- Lumer ED, Edelman GM, and Tononi G.** Neural dynamics in a model of the thalamocortical system. I. Layers, loop and the emergence of fast synchronous rhythms. *Cereb Cortex* 7: 207–227, 1997b.
- Mao BQ, Hamzei-Sichani F, Aronov D, Froemke RC, and Yuste R.** Dynamics of spontaneous activity in neocortical slices. *Neuron* 32: 883–898, 2001.
- Mason A, Nicoll A, and Stratford K.** Synaptic transmission between individual pyramidal neurons of the rat visual cortex in vitro. *J Neurosci* 11: 72–84, 1991.
- Massimini M, Huber R, Ferrarelli F, Hill S, and Tononi G.** The sleep slow oscillation as a traveling wave. *J Neurosci* 24: 6862–6870, 2004.
- Maunsell JH and van Essen DC.** The connections of the middle temporal visual area (MT) and their relationship to a cortical hierarchy in the macaque monkey. *J Neurosci* 3: 2563–2586, 1983.
- McCormick DA.** Neurotransmitter actions in the thalamus and cerebral cortex and their role in neuromodulation of thalamocortical activity. *Prog Neurobiol* 39: 337–388, 1992.
- McCormick DA and Bal T.** Sleep and arousal: thalamocortical mechanisms. *Annu Rev Neurosci* 20: 185–215, 1997.
- McCormick DA, Wang Z, and Huguenard J.** Neurotransmitter control of neocortical neuronal activity and excitability. *Cereb Cortex* 3: 387–398, 1993.
- McLaughlin D, Shapley R, Shelley M, and Wielaard DJ.** A neuronal network model of macaque primary visual cortex (V1): orientation selectivity and dynamics in the input layer 4Calpha. *Proc Natl Acad Sci USA* 97: 8087–8092, 2000.
- Miller KD.** A model for the development of simple cell receptive fields and the ordered arrangement of orientation columns through activity-dependent competition between ON- and OFF-center inputs. *J Neurosci* 14: 409–441, 1994.
- Mittmann T and Alzheimer C.** Muscarinic inhibition of persistent Na^+ current in rat neocortical pyramidal neurons. *J Neurophysiol* 79: 1579–1582, 1998.
- Montero VM.** A quantitative study of synaptic contacts on interneurons and relay cells of the cat lateral geniculate nucleus. *Exp Brain Res* 86: 257–270, 1991.
- Mountcastle VB.** Modality and topographic properties of single neurons of cat's somatic sensory cortex. *J Neurophysiol* 20: 408–434, 1957.
- Mountcastle VB.** The columnar organization of the neocortex. *Brain* 120: 701–722, 1997.
- Mukhametov LM, Rizzolatti G, and Seitun A.** An analysis of the spontaneous activity of lateral geniculate neurons and of optic tract fibers in free moving cats. *Arch Ital Biol* 108: 325–347, 1970.
- Otis TS, De Koninck Y, and Mody I.** Characterization of synaptically elicited GABA_B responses using patch-clamp recordings in rat hippocampal slices. *J Physiol* 463: 391–407, 1993.
- Otis TS and Mody I.** Differential activation of GABA_A and GABA_B receptors by spontaneously released transmitter. *J Neurophysiol* 67: 227–235, 1992.
- Paré D and Lang EJ.** Calcium electrogenesis in neocortical pyramidal neurons in vivo. *Eur J Neurosci* 10: 3164–3170, 1998.
- Payne BR.** Evidence for visual cortical area homologs in cat and macaque monkey. *Cereb Cortex* 3: 1–25, 1993.
- Peters A and Payne BR.** Numerical relationships between geniculocalcarine afferents and pyramidal cell modules in cat primary visual cortex. *Cereb Cortex* 3: 69–78, 1993.

- Peters A and Sethares C.** The organization of double bouquet cells in monkey striate cortex. *J Neurocytol* 26: 779–797, 1997.
- Petersen CC, Grinvald A, and Sakmann B.** Spatiotemporal dynamics of sensory responses in layer 2/3 of rat barrel cortex measured in vivo by voltage-sensitive dye imaging combined with whole-cell voltage recordings and neuron reconstructions. *J Neurosci* 23: 1298–1309, 2003.
- Pinault D and Deschenes M.** Voltage-dependent 40-Hz oscillations in rat reticular thalamic neurons in vivo. *Neuroscience* 51: 245–258, 1992.
- Press WH, Flannery BP, Teukolsky SA, and Vetterling WT.** *Numerical Recipes in C* (2nd ed.). Cambridge, UK: Cambridge Univ. Press, 1992.
- Rakic P.** A small step for the cell, a giant leap for mankind: a hypothesis of neocortical expansion during evolution. *Trends Neurosci* 18: 383–388, 1995.
- Robinson RB and Siegelbaum SA.** Hyperpolarization-activated cation currents: from molecules to physiological function. *Annu Rev Physiol* 65: 453–480, 2003.
- Robson JA.** The morphology of corticofugal axons to the dorsal lateral geniculate nucleus in the cat. *J Comp Neurol* 216: 89–103, 1983.
- Rockland KS.** Laminar distribution of neurons projecting from area V1 to V2 in macaque and squirrel monkeys. *Cereb Cortex* 2: 38–47, 1992.
- Rockland KS and Knutson T.** Feedback connections from area MT of the squirrel monkey to areas V1 and V2. *J Comp Neurol* 425: 345–368, 2000.
- Rockland KS and Pandya DN.** Laminar origins and terminations of cortical connections of the occipital lobe in the rhesus monkey. *Brain Res* 179: 3–20, 1979.
- Rockland KS, Saleem KS, and Tanaka K.** Divergent feedback connections from areas V4 and TEO in the macaque. *Vis Neurosci* 11: 579–600, 1994.
- Rockland KS and Van Hoesen GW.** Direct temporal-occipital feedback connections to striate cortex (V1) in the macaque monkey. *Cereb Cortex* 4: 300–313, 1994.
- Rockland KS and Virga A.** Terminal arbors of individual “feedback” axons projecting from area V2 to V1 in the macaque monkey: a study using immunohistochemistry of anterogradely transported Phaseolus vulgaris-leucoagglutinin. *J Comp Neurol* 285: 54–72, 1989.
- Rosenquist A.** Connections of visual cortical areas in the cat. In: *Cerebral Cortex*, edited by Peters A and Jones E. New York: Plenum, 1985, p. 81–117.
- Rosier AM, Arckens L, Orban GA, and Vandesande F.** Laminar distribution of NMDA receptors in cat and monkey visual cortex visualized by [³H]-MK-801 binding. *J Comp Neurol* 335: 369–380, 1993.
- Salin PA and Bullier J.** Corticocortical connections in the visual system: structure and function. *Physiol Rev* 75: 107–154, 1995.
- Sanchez-Vives MV and McCormick DA.** Cellular and network mechanisms of rhythmic recurrent activity in neocortex. *Nat Neurosci* 3: 1027–1034, 2000.
- Shadlen MN and Newsome WT.** The variable discharge of cortical neurons: implications for connectivity, computation, and information coding. *J Neurosci* 18: 3870–3896, 1998.
- Sherman SM and Guillery RW.** *Exploring the Thalamus*. San Diego, CA: Academic Press, 2001.
- Shipp S and Zeki S.** The organization of connections between areas V5 and V2 in macaque monkey visual cortex. *Eur J Neurosci* 1: 333–354, 1989.
- Shu Y, Hasenstaub A, and McCormick DA.** Turning on and off recurrent balanced cortical activity. *Nature* 423: 288–293, 2003.
- Silva LR, Amitai Y, and Connors BW.** Intrinsic oscillations of neocortex generated by layer 5 pyramidal neurons. *Science* 251: 432–435, 1991.
- Snodderly DM and Gur M.** Organization of striate cortex of alert, trained monkeys (*Macaca fascicularis*): ongoing activity, stimulus selectivity, and widths of receptive field activating regions. *J Neurophysiol* 74: 2100–2125, 1995.
- Softky WR and Koch C.** The highly irregular firing of cortical cells is inconsistent with temporal integration of random EPSPs. *J Neurosci* 13: 334–350, 1993.
- Somers DC, Nelson SB, and Sur M.** An emergent model of orientation selectivity in cat visual cortical simple cells. *J Neurosci* 15: 5448–5465, 1995.
- Stafstrom CE, Schwintz PC, and Crill WE.** Repetitive firing in layer V neurons from cat neocortex *in vitro*. *J Neurophysiol* 52: 264–277, 1984.
- Steriade M.** Corticothalamic resonance, states of vigilance and mentation. *Neuroscience* 101: 243–276, 2000.
- Steriade M.** The corticothalamic system in sleep. *Front Biosci* 8: d878–d899, 2003.
- Steriade M, Nunez A, and Amzica F.** A novel slow (<1 Hz) oscillation of neocortical neurons in vivo: depolarizing and hyperpolarizing components. *J Neurosci* 13: 3252–3265, 1993.
- Steriade M and Timofeev I.** Neuronal plasticity in thalamocortical networks during sleep and waking oscillations. *Neuron* 37: 563–576, 2003.
- Steriade M, Timofeev I, and Grenier F.** Natural waking and sleep states: a view from inside neocortical neurons. *J Neurophysiol* 85: 1969–1985, 2001.
- Stern P, Edwards FA, and Sakmann B.** Fast and slow components of unitary EPSCs on stellate cells elicited by focal stimulation in slices of rat visual cortex. *J Physiol* 449: 247–278, 1992.
- Timofeev I, Grenier F, Bazhenov M, Sejnowski TJ, and Steriade M.** Origin of slow cortical oscillations in deafferented cortical slabs. *Cereb Cortex* 10: 1185–1199, 2000.
- Timofeev I and Steriade M.** Low-frequency rhythms in the thalamus of intact-cortex and decorticated cats. *J Neurophysiol* 76: 4152–4168, 1996.
- Tononi G and Cirelli C.** Sleep and synaptic homeostasis: a hypothesis. *Brain Res Bull* 62: 143–150, 2003.
- Traub RD, Cunningham MO, Gloveli T, LeBeau FE, Bibbig A, Buhl EH, and Whittington MA.** GABA-enhanced collective behavior in neuronal axons underlies persistent gamma-frequency oscillations. *Proc Natl Acad Sci USA* 100: 11047–11052, 2003.
- Tsodyks M, Kenet T, Grinvald A, and Arieli A.** Linking spontaneous activity of single cortical neurons and the underlying functional architecture. *Science* 286: 1943–1946, 1999.
- Tsodyks MV and Markram H.** The neural code between neocortical pyramidal neurons depends on neurotransmitter release probability. *Proc Natl Acad Sci USA* 94: 719–723, 1997.
- Ulrich D and Huguenard JR.** Nucleus-specific chloride homeostasis in rat thalamus. *J Neurosci* 17: 2348–2354, 1997.
- Van Essen DC, Anderson CH, and Felleman DJ.** Information processing in the primate visual system: an integrated systems perspective. *Science* 255: 419–423, 1992.
- van Vreeswijk C and Sompolinsky H.** Chaos in neuronal networks with balanced excitatory and inhibitory activity. *Science* 274: 1724–1726, 1996.
- Vargas-Caballero M and Robinson HP.** A slow fraction of Mg²⁺ unblock of NMDA receptors limits their contribution to spike generation in cortical pyramidal neurons. *J Neurophysiol* 89: 2778–2783, 2003.
- Vautrin J and Barker JL.** Presynaptic quantal plasticity: Katz’s original hypothesis revisited. *Synapse* 47: 184–199, 2003.
- Wang X and Lambert NA.** Membrane properties of identified lateral and medial perforant pathway projection neurons. *Neuroscience* 117: 485–492, 2003.
- Weber JT, Huerta MF, Kaas JH, and Harting JK.** The projections of the lateral geniculate nucleus of the squirrel monkey: studies of the interlaminar zones and the S layers. *J Comp Neurol* 213: 135–145, 1983.
- White EL and Keller A.** *Cortical Circuits: Synaptic Organization of the Cerebral Cortex—Structure, Function, and Theory*. Boston, MA: Birkhauser, 1989.
- Whittington MA, Traub RD, Kopell N, Ermentrout B, and Buhl EH.** Inhibition-based rhythms: experimental and mathematical observations on network dynamics. *Int J Psychophysiol* 38: 315–336, 2000.
- Wimbauer S, Wenisch OG, Miller KD, and van Hemmen JL.** Development of spatiotemporal receptive fields of simple cells: I. Model formulation. *Biol Cybern* 77: 453–461, 1997a.
- Wimbauer S, Wenisch OG, van Hemmen JL, and Miller KD.** Development of spatiotemporal receptive fields of simple cells: II. Simulation and analysis. *Biol Cybern* 77: 463–477, 1997b.
- Wiser AK and Callaway EM.** Contributions of individual layer 6 pyramidal neurons to local circuitry in macaque primary visual cortex. *J Neurosci* 16: 2724–2739, 1996.
- Wiser AK and Callaway EM.** Ocular dominance columns and local projections of layer 6 pyramidal neurons in macaque primary visual cortex. *Vis Neurosci* 14: 241–251, 1997.
- Worgötter F and Koch C.** A detailed model of the primary visual pathway in the cat: comparison of afferent excitatory and intracortical inhibitory connection schemes for orientation selectivity. *J Neurosci* 11: 1959–1979, 1991.
- Zeki S and Shipp S.** Modular connections between areas V2 and V4 of macaque monkey visual cortex. *Eur J Neurosci* 1: 494–506, 1989.
- Zucker RS and Regehr WG.** Short-term synaptic plasticity. *Annu Rev Physiol* 64: 355–405, 2002.